

Notes on the primal-dual algorithm for convex optimization applied to X-ray tomographic image reconstruction

Emil Y. Sidky and X. Pan

Department of Radiology, University of Chicago, MC-2026, 5841 S. Maryland Ave., Chicago, Illinois 60637

E-mail: sidky@uchicago.edu, xpan@uchicago.edu

17 March 2026

Abstract. The purpose of these notes is to provide background on understanding the primal-dual algorithm of Chambolle and Pock [1] for imaging scientists. The presentation focuses on providing intuition and an algorithmic system that is amenable to pre-conditioning. The document aims to be self-contained, providing background on the essential facts of non-smooth convex analysis.[2]

1. Introduction

In Ref. [3], we demonstrated how to implement the primal-dual (CPPD) algorithm of Chambolle and Pock [1] for solving non-smooth convex optimization problems of interest to X-ray tomographic image reconstruction. The CPPD algorithm has proven useful in that it allows a great deal of flexibility in formulating convex optimization problems that allow for a variety of data models, regularization terms, and image constraints. These notes focus on a simplified CPPD system, i.e. no $G(x)$ function, which allows for a simple preconditioning technique.

Future updates of this document will focus on including the $G(x)$ function, how to effectively deal with system matrices composed of multiple blocks, and the connection with the alternating direction method of multipliers (ADMM) algorithm [4]. The connection to ADMM is useful for developing solvers for non-convex optimization problems [5].

The main body of these notes presents a fairly direct narrative toward the goal of writing a CPPD algorithm for total variation (TV) regularized least-squares image reconstruction, which includes preconditioning. The appendices have supporting discussions on some of the convex analysis concepts, additional derivations, and numerical experiments. Please contact us if you have any questions, comments, or spotted errors.

2. Methods

2.1. CPPD background

The CPPD algorithm is designed to solve the generic convex optimization problem

$$x^* = \underset{x}{\operatorname{argmin}} F(Ax), \quad (1)$$

where x is a n -dimensional vector; A is a $m \times n$; $F(\cdot)$ is a simple, convex function that is possibly non-smooth. This problem is actually a special case of what is considered in Ref. [1], which also considered an additional convex term $G(x)$. The minimization in Eq. (1) encompasses many optimization problems of interest for X-ray CT.

The difficulty in solving Eq. (1) results from the composition of F with a large linear transform A , where large means that it is only computationally feasible to calculate matrix-vector products such as Ax and matrix operations on A , such as diagonalization, is not feasible. The CPPD algorithm results from converting Eq. (1) to a saddle point problem, where the convex function F appears in a different than the linear transform A . The derivation of the saddle point problem goes as follows:

The minimization in Eq. (1) is equivalent to the equality-constrained minimization

$$\min_{x,y} F(y) \text{ such that } y = Ax,$$

where the splitting variable, y , is a m -dimensional vector. This in turn can be converted to an unconstrained saddle point problem by forming the Lagrangian L

$$L(x, y, \lambda) = F(y) + \lambda^\top (Ax - y),$$

where λ , also a m -dimensional vector, is the Lagrange multiplier or dual variable. The saddle point problem optimizing L is

$$\min_{x,y} \max_{\lambda} L(x, y, \lambda), \quad (2)$$

and the solution can be identified formally by setting the gradient of L to zero, see Appendix A,

$$\partial_x L(x, y, \lambda) = A^\top \lambda = 0, \quad (3)$$

$$\partial_y L(x, y, \lambda) = \partial F(y) - \lambda = 0, \quad (4)$$

$$\partial_\lambda L(x, y, \lambda) = Ax - y = 0, . \quad (5)$$

We will use the first and third of these equations to provide convergence checks for the CPPD algorithm. The widely used alternating direction method of multipliers (ADMM) algorithm solves this system of equations with update steps derived from a modified Lagrangian, where a term quadratic in $\|Ax - y\|$ is added to the Lagrangian $L(x, y, \lambda)$ [4].

For the CPPD algorithm, the size of the saddle point problem in Eq. (2) is reduced by carrying out the minimization over y . The second condition for the solution of this problem, Eq. (4), can be solved directly if F is a simple function. The expression in Eq. (4) originated from the gradient of the terms in $L(x, y, \lambda)$ that involved y . Isolating the minimization over y from Eq. (2) yields

$$\min_y \{F(y) - \lambda^\top y\},$$

which is essentially the Legendre-Fenchel transform of $F(y)$, see Appendix C:

$$\min_y \{F(y) - \lambda^\top y\} = -\max_y \{\lambda^\top y - F(y)\} \equiv -F^*(\lambda).$$

Recall that for convex $F(y)$

$$\begin{aligned} F^*(\lambda) &\equiv \max_y \{\lambda^\top y - F(y)\}, \\ F(y) &\equiv \max_\lambda \{y^\top \lambda - F^*(\lambda)\}. \end{aligned}$$

If $F^*(\lambda)$ is easily computed, the saddle point problem in Eq. (2) can be reduced to

$$\min_x \max_\lambda \{\lambda^\top Ax - F^*(\lambda)\}. \quad (6)$$

For many optimization problems of interest for CT image reconstruction, F^* can be derived analytically.

2.2. Heuristics for the CPPD algorithm and preconditioning

The CPPD algorithm solves the saddle point problem in Eq. (6), but the form of the algorithm is difficult to understand at an intuitive level. In addition to the development of this section, please refer also to Appendix E. Intuition on the algorithm can be acquired by focusing only on the saddle term

$$s(x, \lambda) = \lambda^\top Ax.$$

The critical point of this potential is found by setting its gradient to zero. If A is full-rank and invertible, there is only one critical point at $x_{\text{crit}} = 0, \lambda_{\text{crit}} = 0$. More generally, the critical points satisfy

$$\begin{aligned} Ax_{\text{crit}} &= 0, \\ A^\top \lambda_{\text{crit}} &= 0. \end{aligned}$$

That the critical point is a saddle point is seen by computing the Hessian

$$H_s = \begin{pmatrix} \frac{\partial^2}{\partial x^2} s(x, \lambda) & \frac{\partial^2}{\partial \lambda \partial x} s(x, \lambda) \\ \frac{\partial^2}{\partial x \partial \lambda} s(x, \lambda) & \frac{\partial^2}{\partial \lambda^2} s(x, \lambda) \end{pmatrix} = \begin{pmatrix} 0 & A^\top \\ A & 0 \end{pmatrix}.$$

The trace of the Hessian is zero; therefore the sum of eigenvalues is zero. As a result, there must be negative and positive eigenvalues, meaning that $s(x, \lambda)$ has directions of negative and positive curvature. Thus, $(x_{\text{crit}}, \lambda_{\text{crit}})$ is a saddle point of $s(x, \lambda)$.

2.2.1. Forward Euler iteration A saddle point solver should be able to find the critical saddle point(s) from arbitrary initialization (x_0, λ_0) . Because Eq. (6) calls for minimization over x and maximization over λ , a first attempt at an algorithm might involve taking a step in the direction of $-\partial_x s$ and $\partial_\lambda s$. Forming the forward Euler iteration yields

$$x_{k+1} = x_k - \alpha A^\top \lambda_k, \quad (7)$$

$$\lambda_{k+1} = \lambda_k + \alpha Ax_k, \quad (8)$$

where α is a step-size parameter. This iteration, however, is unstable for all step-sizes α ; this can be shown by computing the magnitude of the solution estimate, $\|(x_{k+1}, \lambda_{k+1})^\top\|$, in terms of $\|(x_k, \lambda_k)^\top\|$. The ratio of the former to the latter is greater than one for any $\alpha \neq 0$. Thus, the iteration in Eqs. (7) and (8) spirals away from the critical saddle point(s) unless it is initialized with the solution, i.e. a critical saddle point.

2.2.2. Backward Euler iteration The second attempt at an algorithm is to use backward Euler iteration, where the step direction is computed based on the gradients at the updated point instead. For the $s(x, \lambda)$ saddle-point solver this update is written

$$x_{k+1} = x_k - \alpha A^\top \lambda_{k+1}, \quad (9)$$

$$\lambda_{k+1} = \lambda_k + \alpha A x_{k+1}, \quad (10)$$

where the difference with the forward Euler iteration is in the last terms of both update equations. Those terms use λ_{k+1} and x_{k+1} instead of λ_k and x_k . Bringing all terms involving $k+1$ to the left-side, the backward Euler update equations become

$$\begin{pmatrix} 1 & \alpha A^\top \\ -\alpha A & 1 \end{pmatrix} \begin{pmatrix} x_{k+1} \\ \lambda_{k+1} \end{pmatrix} = \begin{pmatrix} x_k \\ \lambda_k \end{pmatrix}. \quad (11)$$

This iteration can be shown to converge to a critical point of $s(x, \lambda)$ for any positive step-size, α . The problem with this algorithm, however, is that each update computation involves solving the linear system in Eq. (11). If A is a large matrix, this computation may have to be addressed with an iterative linear systems solver, and thus the whole algorithm would involve a "loop inside of a loop", which could be computationally infeasible.

2.2.3. Approximate backward Euler iteration One of the key insights of the CPPD algorithm [1] is to use the backward Euler step in an approximate fashion by extrapolating x from the previous two iterations

$$\bar{x}_{k+1} = x_k + \theta(x_k - x_{k-1}), \quad (12)$$

$$\lambda_{k+1} = \lambda_k + \alpha A \bar{x}_{k+1}, \quad (13)$$

$$x_{k+1} = x_k - \alpha A^\top \lambda_{k+1}, \quad (14)$$

where $\theta \in [0, 1]$ is the extrapolation parameter; for the following sections of the article we employ $\theta = 1$, which extrapolates x_{k+1} exactly if x_k is a linear function of k . By using \bar{x}_{k+1} instead of x_{k+1} in Eq. (13), it is no longer necessary to solve a linear system for each iteration; all update steps can be computed directly with matrix vector products.

Even though this scheme is reasoned heuristically, its convergence is rigorously proven in Ref. [1], but unlike the backward iteration case where any α yields convergence, the condition on α here is

$$\alpha < 1/\|A\|_2,$$

where the matrix norm $\|A\|_2$ is the largest singular value of A ; in practice, setting $\alpha = 1/\|A\|_2$ usually results in a convergent iteration. The dual update, Eq. (13), and the primal update, Eq. (14), can also employ different stepsizes, σ and τ , respectively, as long as they satisfy

$$\sigma\tau < 1/\|A\|_2^2,$$

where again this condition, in practice, can include the equality. Implementing the different step sizes and reordering the steps yields

$$x_{k+1} = x_k - \tau A^\top \lambda_k, \quad (15)$$

$$\bar{x}_{k+1} = x_{k+1} + \theta(x_{k+1} - x_k), \quad (16)$$

$$\lambda_{k+1} = \lambda_k + \sigma A \bar{x}_{k+1}. \quad (17)$$

This form is slightly more convenient in that it only requires x_k and λ_k to compute values for the $k + 1$ -iteration.

2.2.4. Generalization to matrix-mapping steps The CPPD iteration is also shown to be a generalization of the proximal point algorithm [6, 4]. This generalization allows for matrix-mapping steps, where σ and τ are replaced with symmetric positive matrices Σ and T

$$x_{k+1} = x_k - T A^\top \lambda_k, \quad (18)$$

$$\bar{x}_{k+1} = 2x_{k+1} - x_k, \quad (19)$$

$$\lambda_{k+1} = \lambda_k + \Sigma A \bar{x}_{k+1}, \quad (20)$$

where we only consider $\theta = 1$. For this algorithm to converge, the condition on the matrices Σ and T is arrived at through the matrix

$$B = \begin{pmatrix} T^{-1} & -A^\top \\ -A & \Sigma^{-1} \end{pmatrix}.$$

For convergence, B should be a positive definite matrix, see Appendix F. Using the Schur complement, this condition on B reduces to either

$$T^{-1} - A^\top \Sigma A > 0 \quad (21)$$

or

$$\Sigma^{-1} - A T A^\top > 0, \quad (22)$$

where the inequalities are shorthand for indicating that the matrix on the left is positive definite. Again, in practice, we can use the equality on either of these conditions. In particular, take

$$\Sigma^{-1} = A T A^\top. \quad (23)$$

This relation between the dual and primal matrix step-mappings proves useful for designing non-diagonal step-preconditioners.

2.2.5. Preconditioning based on inverse of $(A^\top A)$ To demonstrate perfect preconditioning, take the case

$$T = (\rho A^\top A)^{-1}, \quad (24)$$

and

$$\Sigma = \rho I, \quad (25)$$

where I is the identity matrix; the step-size ratio parameter ρ is a positive scalar; and $A^\top A$ is assumed invertible. This choice of T and Σ satisfies Eq. (23). Substituting this T expression into Eq.(18) yields

$$x_{k+1} = x_k - (1/\rho)A^{-1}\lambda_k;$$

and multiplying through by A and setting $u = Ax$, we have

$$u_{k+1} = u_k - (1/\rho)\lambda_k.$$

Combining Eqs. (19), (20), and (25) yields

$$\lambda_{k+1} = \lambda_k + \rho(2u_{k+1} - u_k),$$

where again $u = Ax$ is used. Simplifying the expression for λ_{k+1} reduces the update equations to

$$\begin{aligned} u_{k+1} &= u_k - (1/\rho)\lambda_k, \\ \lambda_{k+1} &= \rho(u_k - (1/\rho)\lambda_k). \end{aligned}$$

Direct computation shows that this iteration will terminate in two steps for any $u_0 = Ax_0$, λ_0 , and $\rho > 0$ with the result $u_2 = Ax_2 = 0$ and $\lambda_2 = 0$. The parameter ρ has no effect on the number of iterations, here, but it proves useful for the general CPPD iteration.

For large-scale A , it may not be feasible or possible to compute $(A^\top A)^{-1}$, and the convergence in two steps is lost once the more general saddle point problem in Eq. (6) is considered. But the presented argument is a heuristic for use of an approximate inverse for T

$$T \approx (A^\top A)^{-1}$$

as a non-diagonal step-preconditioner. If T is a matrix that is only an approximate inverse of $(A^\top A)^{-1}$ it will also be infeasible to compute Σ using Eq. (23). Instead it is more practical to assume Σ is diagonal and choose it so it satisfies the inequality in Eq. (22). This is accomplished by setting the diagonal elements of Σ to a value less than the largest singular value of ATA^\top ; the largest singular value can be obtained by the power method. In some cases it is more convenient to do power iteration with the matrix $TA^\top A$, which has the same largest eigenvalue as the matrix ATA^\top . The step-size ratio parameter ρ can still be used when T is an approximate inverse of $(A^\top A)^{-1}$ because it results from multiplying both sides of the inequality in Eq. (22) by ρ .

2.3. Heuristic derivation of CPPD

The update steps in Eqs. (18) - (20) combined with strategies for setting the step matrices Σ and T only address solution of the bilinear saddle point optimization $\lambda^\top Ax$. The extension to the main problem of interest Eq. (6) involves accounting for the additional concave potential term $-F^*(\lambda)$. We run through the complete argument with backward Euler iteration once more using the step matrices from the beginning.

Repeating the saddle problem of interest

$$\min_x \max_\lambda \{ \lambda^\top Ax - F^*(\lambda) \},$$

the x and λ updates for backward Euler iteration are

$$\begin{aligned} \lambda_{k+1} &= \lambda_k + \Sigma (Ax_{k+1} - \partial F^*(\lambda_{k+1})), \\ x_{k+1} &= x_k - TA^\top \lambda_{k+1} \end{aligned}$$

where Σ and T are symmetric positive definite matrices, i.e. positive eigenvalues. Working toward the CPPD algorithm, x_{k+1} in the λ update is replaced by an extrapolation and the differential term is moved to the left-hand side.

$$\begin{aligned}\bar{x}_{k+1} &= 2x_k - x_{k-1}, \\ \Sigma \partial F^*(\lambda_{k+1}) + \lambda_{k+1} &= \lambda_k + \Sigma A \bar{x}_{k+1} \\ x_{k+1} &= x_k - T A^\top \lambda_{k+1}.\end{aligned}\tag{26}$$

The λ -update equation is implicit in the desired update variable λ_{k+1} , and to obtain it explicitly involves the proximal mapping, also known as the resolvent of $\Sigma \partial F^*$, see Appendix F.

The desired proximal mapping is expressed as the argument of a minimization problem, which can be derived in a few steps. Regarding the right-hand side of the λ -update as an argument to the desired mapping

$$\lambda_{\text{arg}} = \lambda_k + \Sigma A \bar{x}_{k+1},$$

this update equation becomes

$$\Sigma \partial F^*(\lambda_{k+1}) + \lambda_{k+1} = \lambda_{\text{arg}}.\tag{27}$$

Dropping the $k+1$ subscript from λ_{k+1} for clarity, rearranging terms, and multiplying through by Σ^{-1} yields

$$\partial F^*(\lambda) + \Sigma^{-1}(\lambda - \lambda_{\text{arg}}) = 0,$$

where inversion of Σ is possible because it is assumed to be a symmetric positive definite matrix. The left-hand side can be written as a total differential

$$\frac{\partial}{\partial \lambda} \left(F^*(\lambda) + \frac{1}{2}(\lambda - \lambda_{\text{arg}})^\top \Sigma^{-1}(\lambda - \lambda_{\text{arg}}) \right) = 0.\tag{28}$$

The second term inside the differential operation is a quadratic distance function with metric Σ^{-1}

$$\|\lambda - \lambda_{\text{arg}}\|_{\Sigma^{-1}}^2 \equiv (\lambda - \lambda_{\text{arg}})^\top \Sigma^{-1}(\lambda - \lambda_{\text{arg}}),$$

because Σ^{-1} is also a symmetric positive definite matrix. Both the distance function and F^* are convex functions, so their sum is also a convex function. Accordingly, Eq. (28) can be viewed as specifying the minimizer of the function inside the differentiation; setting the gradient of a convex function to zero identifies its minimizer. Thus, the explicit expression for λ_{k+1} from Eq. (27) is

$$\lambda_{k+1} = \underset{\lambda}{\operatorname{argmin}} \left\{ F^*(\lambda) + \frac{1}{2} \|\lambda - \lambda_{\text{arg}}\|_{\Sigma^{-1}}^2 \right\}.\tag{29}$$

Technically, Eq. (28) only applies when F^* is smooth, but Eq. (29) does apply for the desired case where F^* is convex and possibly non-smooth. For general Σ , the problem in Eq. (29) can be challenging to solve analytically. Thus, for the CPPD framework considered here, Σ is restricted to a diagonal matrix with all diagonal values set to the scalar σ , i.e.

$$\Sigma = \sigma I,$$

where I is the identity matrix. Equation (29) becomes

$$\lambda_{k+1} = \operatorname{argmin}_{\lambda} \left\{ F^*(\lambda) + \frac{1}{2\sigma} \|\lambda - \lambda_{\operatorname{arg}}\|_2^2 \right\} \equiv \operatorname{prox}_{\sigma F^*}(\lambda_{\operatorname{arg}}),$$

where the argmin problem is defined as the prox mapping.

Using the explicit λ -update equation and reordering the steps so that the x -update comes first, the CPPD update equations from Eq. (26) become

$$\begin{aligned} x^{(k+1)} &= x^{(k)} - TA^\top \lambda^{(k)}, \\ \bar{x}^{(k+1)} &= 2x^{(k+1)} - x^{(k)}, \\ \lambda^{(k+1)} &= \operatorname{prox}_{\sigma F^*}(\lambda^{(k)} + \sigma \bar{x}^{(k+1)}). \end{aligned} \tag{30}$$

In this algorithm framework, T is still allowed to be a general positive definite matrix. For the basic CPPD implementation as discussed in the original paper on the primal-dual algorithm [1], T is a diagonal matrix

$$T = \tau I,$$

and the condition for convergence is

$$\tau\sigma \leq 1/\|A\|_2^2.$$

More generally, when T is a positive definite matrix, the condition for convergence is

$$1/\sigma \geq \|TA^\top A\|_2.$$

We demonstrate examples of both of these choices in Sec. 3. The CPPD update is proved to converge only in the case of strict inequality, but empirically, equality leads to convergence. A useful choice of step-sizes discussed by Pock and Chambolle [7] avoids the power method and allows for fast step-size computation, see Appendix G. In the same Appendix, we also present a useful implementation of a non-diagonal step-matrix T designed for image reconstruction problems in X-ray tomography with possibly non-standard scan geometries.

3. Results

In this section, instances of the CPPD algorithm are demonstrated on optimization problems relevant to CT image reconstruction. The goals of the studies are to demonstrate use of the CPPD algorithm, to characterize the impact of algorithm parameters, to illustrate convergence, and, in general, to motivate the necessity of comprehensive empirical studies. All presented studies focus on sampling sufficiency, and the simulation studies model breast CT. Various scanning geometries are considered and all of the simulations take the form of an ‘‘inverse crime’’ [8] study, where the projection data are perfectly consistent with object and data models.

The inverse crime studies have multiple purposes. First, they present a stringent test for correct algorithm implementation, because we know that the data discrepancy can be driven to zero. Second, this is the only practical way to demonstrate sampling sufficiency for the discrete-to-discrete data model used in iterative image reconstruction; if the sampling is sufficient the converged solution will be the test phantom, and if not, the converged solution will differ from the test phantom. Third, the inverse crime set up is excellent for empirical demonstration of algorithm convergence rate, which is useful for parameter tuning and optimization solver comparison.

3.1. Optimization problems and solvers

The optimization problems considered are designed to invert the discrete-to-discrete data-model.

$$Xf = g,$$

where X represents discrete-to-discrete projection; f is the vector of image pixels; and g is a vector of projection data. In implementing X this matrix is the product

$$X = X_{\text{grid}}M_{\text{FOV}}, \quad (31)$$

where M_{FOV} is a diagonal matrix with entries 1 and 0 on the diagonal that correspond respectively to pixels inside and outside of the FOV; X_{grid} represents projection of the whole rectangular image grid. In the following studies, g is taken to be noiseless projection of the discretized digital phantom using the system matrix X .

Least-squares

Two optimization problems are considered for inversion of the data model. The first is formulated as a least-squares (LSQ) optimization

$$f^* = \operatorname{argmax}_f \frac{1}{2} \|Xf - g\|_2^2,$$

where the solution f^* is arrived at only through the available projection data. In inverse crime studies, if f^* matches the test phantom, this is evidence that the matrix X encodes a CT system that is sufficiently sampled. Inversion by LSQ provides the opportunity to demonstrate the CPPD algorithm on a ubiquitous optimization problem that is amenable to solution by many standard algorithms.

Algorithm 1 Pseudocode for CPPD-LSQ inner loop for iteration k . See Appendix I for derivation of the CPPD-LSQ updates. The step length parameters are set to $\sigma = \rho/L$ and $\tau = 1/(\rho L)$, where $L = \|X\|_2$. The step-ratio parameter ρ and iteration number k_{max} are varied in the studies. Although warm-starting is possible, we do not consider this here and initialize $f^{(0)} = 0$ and $\lambda^{(0)} = 0$.

- 1: $f^{(k+1)} \leftarrow f^{(k)} - \tau X^\top \lambda^{(k)}$
 - 2: $\bar{f} \leftarrow 2f^{(k+1)} - f^{(k)}$
 - 3: $\lambda^{(k+1)} \leftarrow (\lambda^{(k)} + \sigma(X\bar{f} - g)) / (1 + \sigma)$
-

Algorithm 2 Pseudocode for GD-LSQ inner loop for iteration k . The step length is determined by $\alpha \in (0, 2)$ and L , where $L = \|X\|_2$. The parameters α and iteration number k_{max} are varied in the studies. We initialize $f^{(0)} = 0$.

- 1: $f^{(k+1)} \leftarrow f^{(k)} - (\alpha/L^2)X^\top(Xf^{(k)} - g)$
-

The derivation of the CPPD algorithm for least-squares optimization (CPPD-LSQ) is presented in Appendix I, and the pseudo-code is listed in Algorithm 1. We compare

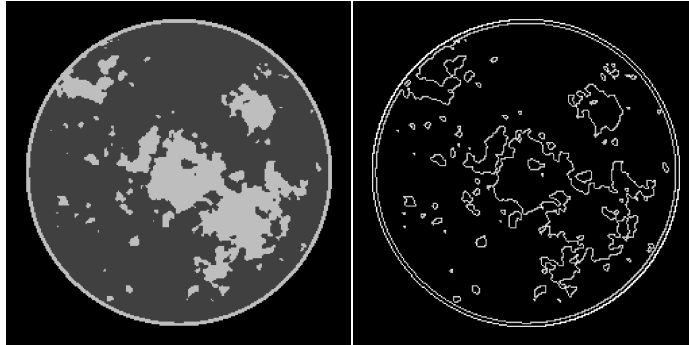


Figure 1. Computerized breast phantom and its gradient magnitude image (GMI). In the GMI it is apparent that the phantom has a high degree of gradient sparsity even though the tissue borders are highly irregular. The gradient sparsity is useful for testing ideal recovery from under-sampled data by use of sparsity regularization with TV. The attenuation values in this phantom are taken to be 0.194 cm^{-1} and 0.233 cm^{-1} for fat and fibro-glandular tissue, respectively. The phantom and its GMI are shown in a gray scale window of $[0.174, 0.253] \text{ cm}^{-1}$ and $[0.0, 0.05] \text{ cm}^{-1}$, respectively.

performance of CPPD-LSQ with gradient descent applied to the LSQ problem (GD-LSQ), as listed in 2, and to conjugate gradients least-squares, as listed on page 57 of Ref. [9]. The parameters of GD-LSQ and CPPD-LSQ are explained in their respective pseudo-codes. The only parameter varied for CGLS is the total number of iterations; the starting image is initialized to zero and no attempt at pre-conditioning is made. CGLS is chosen because it is the gold-standard solver for large-scale LSQ problems. Basic GD-LSQ, with a fixed step-size, is almost never used in practice because there are many options that are more efficient, see for example Ref. [10], but it provides a common reference point.

Total-variation constrained least-squares

The second optimization problem considered is the total-variation (TV) constrained least-squares (TVCLSQ) problem

$$f^* = \operatorname{argmax}_f \frac{1}{2} \|Xf - g\|_2^2 \text{ such that } \|Df\|_1 \leq \gamma,$$

where D is the discrete gradient matrix operator and γ is the constraint parameter. For inverse crime studies, the phantom is known and γ can be set to the phantom TV value γ_{ph} . This optimization problem is useful for Compressive Sensing [11, 12] investigations, where gradient sparsity is exploited to reduce the scanning effort. In compressive sensing, image recovery is governed by the number of samples, the size of the data, and the sparsity of the object. If the former is sufficiently greater than the latter, the image can be recovered even for configurations with reduced sampling. For CT, reduced sampling usually means reduced numbers of projections or scanning angular range. A theoretical, empirical compressive sensing study for CT was carried out using this optimization problem in Ref. [13]. The CPPD-TVCLSQ pseudo-code is derived in Appendix I where the listing appears in Algorithm 4. Compressive sensing

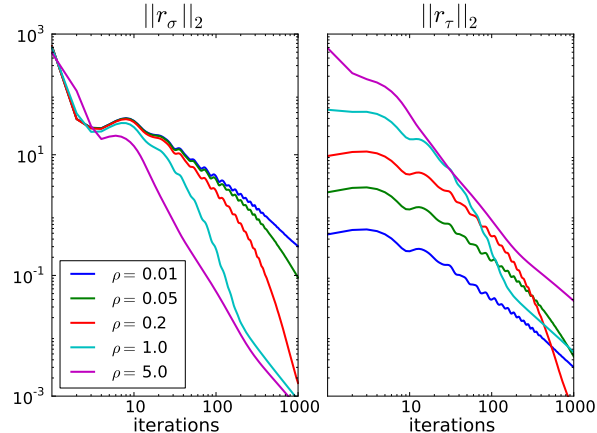


Figure 2. Plots of $\|r_\sigma\|_2$ and $\|r_\tau\|_2$, see Eqs. (H.1) and (H.2) in Appendix H, as a function of iteration number and for different values of the step-size ratio parameter ρ .

has motivated a number of sparsity-exploiting image reconstruction studies in medical imaging [14, 15, 16].

3.2. simulation parameters

The test set-up is based on breast CT in a 2D setting. The phantom is shown in Fig. 1 and it is generated by a phantom model described in Ref. [17]. The phantom and image reconstruction grids are both 256×256 pixels covering an area $18 \text{ cm} \times 18 \text{ cm}$. The simulated CT sampling configuration is circular, fan-beam with varying numbers of projections and scanning arc length. The simulated projections employ a linear detector of 512 bins; the source-to-center distance is 36 cm, and source-to-detector is 72 cm. The detector length is set so that the field-of-view (FOV) has a diameter of 18 cm and matches the inscribed circle of the pixel grid.

The active pixels are those inside the FOV, and their number is 51,468 or approximately 79% of the 256×256 pixels in the square array. The reason that only FOV pixels are selected for reconstruction is to make sure that all active pixels are visible in all projections. Implementation-wise, a masking operation, which multiplies all non-FOV pixels by zero, is applied prior to projection and after back-projection, see Eq. (31).

In the presented empirical studies, three scan configurations are considered: full-sampling, 128 projections over a 2π scanning arc; sparse-view, 32 projections over a 2π scanning arc; and limited angular-range, 128 projections over a $3\pi/4$ scanning arc. For both the full-sampling and limited angular-range scanning configurations the number of samples is 128×512 , which is equal to the pixel grid size of 256×256 . From the perspective of number of samples versus number of unknowns, these configurations represent slight over-sampling, because only 79% of the pixels are active due to the FOV masking. This amount of over-sampling, by itself, presents a challenge. We have found that the X-ray transform matrix conditioning is relatively poor [18], when the number of unknown pixel values is similar to the number of samples, irrespective of scanning arc length. The limited angular-range configuration provides an interesting

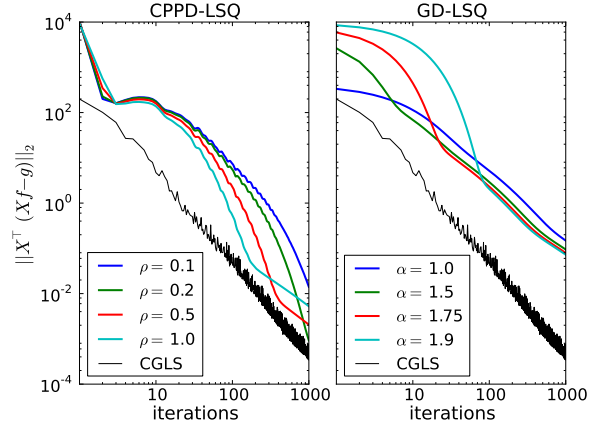


Figure 3. Plots of the LSQ objective function gradient magnitude for CPPD-LSQ, GD-LSQ, and CGLS as a function of iteration number.

test, because it is sufficiently sampled from the perspective of number of unknowns and samples but the corresponding continuous X-ray transform model is known to be insufficiently sampled since the scanning arc length is less than π plus fan-angle. The sparse-view scan configuration is clearly under-sampled if no prior information on the object is exploited, because the number of samples is less than the number of unknown pixel values. For this configuration and phantom, exploiting gradient sparsity is known to be an effective strategy. These sampling conditions are chosen to illustrate various aspects of CPPD convergence.

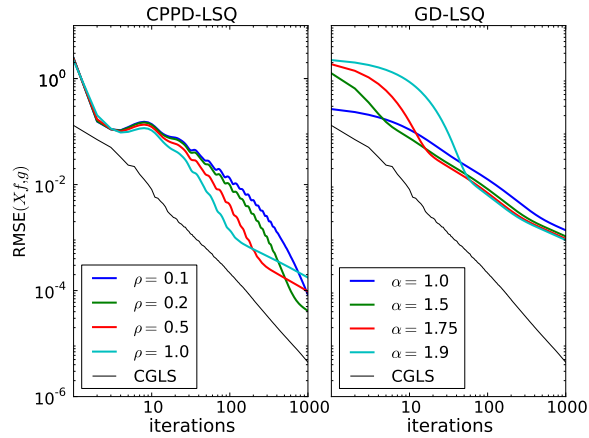


Figure 4. Plots of the LSQ objective function for CPPD-LSQ, GD-LSQ, and CGLS as a function of iteration number.

3.3. Least-squares convergence studies for full-sampling

The convergence plots in Fig. 2 show the splitting gap and transversality evolution for CPPD-LSQ as a function of iteration number for different values of the step-size

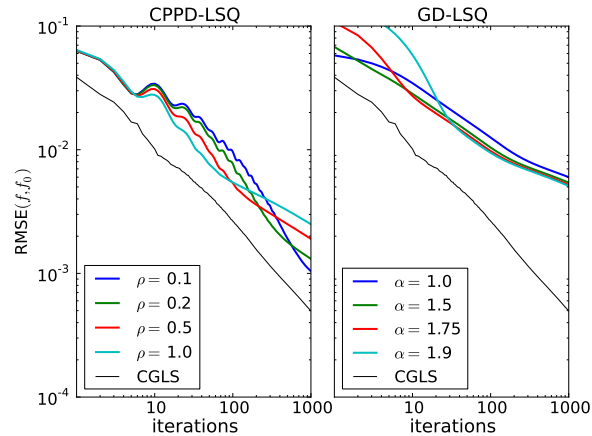


Figure 5. Plots of the image root-mean-square-error (RMSE) discrepancy for CPPD-LSQ, GD-LSQ, and CGLS as a function of iteration number.

ratio ρ , where

$$\rho = \sqrt{\frac{\sigma}{\tau}}.$$

The transversality, r_τ , and splitting gap, r_σ , convergence metrics for CPPD are presented in detail in Appendix H. When ρ is larger than 1, $\sigma > \tau$, and as a general overall trend larger ρ correlates with a faster decrease in $\|r_\sigma\|_2$ while smaller ρ tends to improve convergence in $\|r_\tau\|_2$. Overall the curves from the shown intermediate values of $\rho = 0.2$ and $\rho = 1.0$ seem most promising when considering both convergence plots together.

For the LSQ problem, which has a differentiable objective function, we can also plot the magnitude of the LSQ objective gradient as a function of iteration number. This metric is a complete first-order convergence condition and it allows comparison with GD-LSQ and CGLS. The gradient of the LSQ objective function

$$\phi(f) = \frac{1}{2} \|Xf - g\|_2$$

is

$$\partial\phi(f) = X^\top(Xf - g).$$

The comparison of CPPD-LSQ with GD-LSQ and CGLS is shown in Fig. 3. By this metric and for this particular CT configuration, the convergence rate of CPPD-LSQ is better than GD-LSQ and not as good as CGLS.

Because we are performing an inverse crime study there are also two more convergence metrics available. The LSQ objective value itself can be driven to zero, and the corresponding results are shown in Fig. 4. The LSQ objective function should tend to zero no matter what is the data sampling configuration for consistent data. To test sampling sufficiency, it is necessary to demonstrate convergence of the image estimate to the test phantom. The plots of the image estimate discrepancy in Fig. 5 show curves that all tend to zero, thus the present configuration does provide sampling sufficiency.

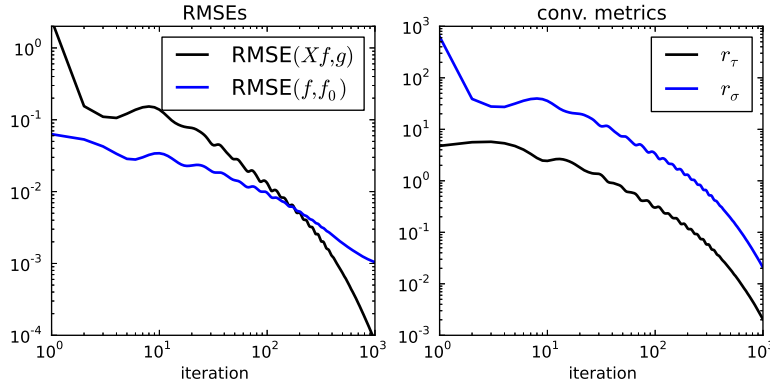


Figure 6. Convergence metrics for CPPD-LSQ for a step-size ratio of $\rho = 0.1$. The left panel shows the image and data RMSE, and the right panel displays the transversality condition and splitting gap.

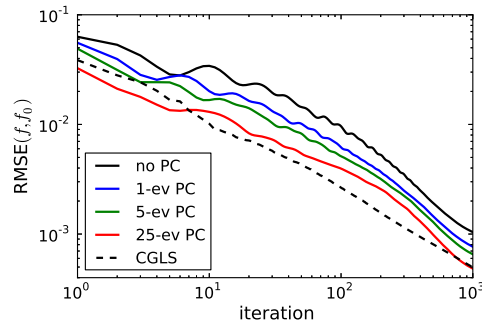


Figure 7. Impact of non-diagonal preconditioning (PC) on image RMSE for CPPD-LSQ applied to image reconstruction for the 128-view data configuration. The legend indicates the number of eigenvectors (ev) of X used in forming the preconditioner. Also shown are the traces for scalar σ and τ , i.e. no preconditioning and generic CGLS.

The convergence curves are all plotted on a log-log scale because all of these quantities are expected to tend to zero. By using a log-log plot, it is possible to visually estimate at which iteration number a desired accuracy can be obtained. Asymptotically, first-order algorithms converge to the solution by a power of the iteration number; a quantity that tends to zero will thus appear linear on a log-log scale when this asymptotic behavior is reached. For the LSQ problem, the metrics r_σ , r_τ , and object gradient magnitude should all tend to zero irrespective of data consistency or sampling. The LSQ objective function tends to zero with perfectly consistent data, and the image RMSE tends to zero with consistent data and sufficient sampling.

Taking in all these curves, there is the general impression that CPPD-LSQ performance in terms of convergence lies somewhere between GD-LSQ and CGLS. The range of interesting ρ settings for CPPD-LSQ appears to be between 0.1 and 1.0. Focusing on the convergence metrics for CPPD-LSQ, they clearly all tend to zero. The ρ -rank-order of the convergence is seen to depend on iteration number and which metric is used. Because the presented results center on inverse crime studies, the image

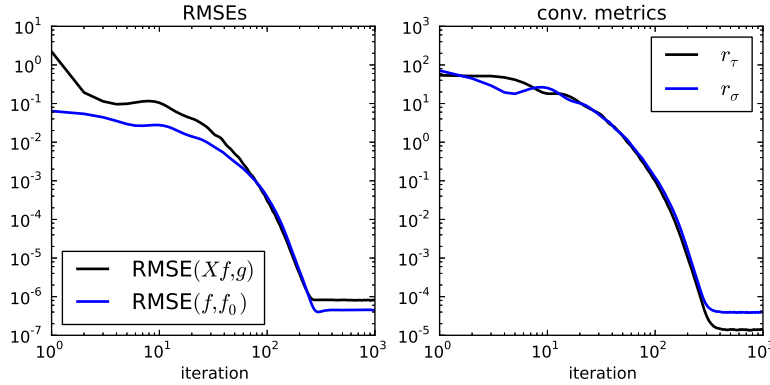


Figure 8. Convergence metrics for CPPD-TVCLSQ for a step-size ratio of $\rho = 1.0$. The left panel shows the image and data RMSE, and the right panel displays the transversality condition and splitting gap.

RMSE metric is most relevant and ρ is selected based on rank-order at 1000 iterations, which is the number of iterations used in the simulations. For the ρ values tested, $\rho = 0.1$ leads to the lowest image RMSE after 1,000 iterations and the corresponding convergence metric traces are displayed in Fig. 6. Whichever convergence metric is used for selecting ρ , it is clear that the convergence rate does depend strongly on ρ and this parameter must be tuned in order to maximize CPPD performance.

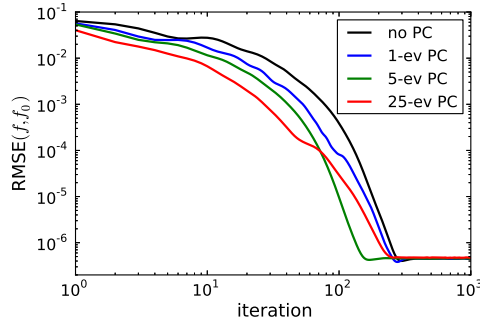


Figure 9. Impact of non-diagonal preconditioning (PC) on image RMSE for CPPD-TVCLSQ applied to image reconstruction for the 128-view data configuration. The legend indicates the number of eigenvectors (ev) of X used in forming the preconditioner. Also shown are the traces for scalar σ and τ , i.e. no preconditioning and generic CGLS.

Improving CPPD-LSQ performance with non-diagonal preconditioning

In case that greater efficiency is needed for the CPPD algorithm, non-diagonal step matrices can be exploited as alluded to in Sec. 2.2.4. To demonstrate such preconditioning, the scalar step-size τ in the first line of Algorithm 1 is replaced by a matrix T , which, in the case of the LSQ problem, is set to an approximate inverse of $X^\top X$. For a low-rank approximate inverse, see Eq. (G.3) in Appendix G, where

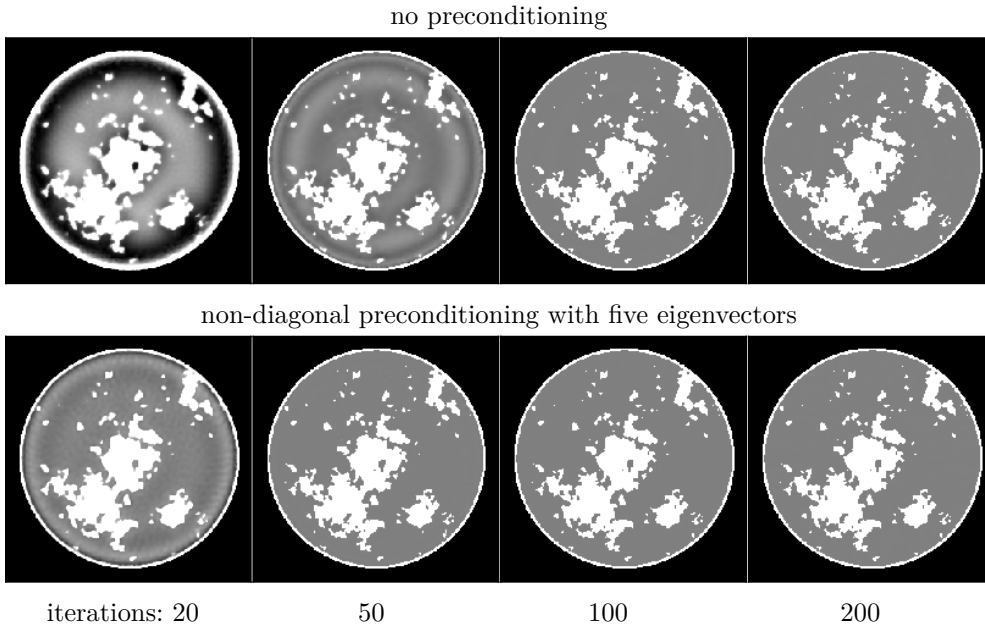


Figure 10. Sequence of image estimates for different iteration numbers of CPPD-TVCLSQ. Top row shows results for no preconditioning, and the bottom row displays images for non-diagonal preconditioning. The gray scale is $[0.174, 0.214] \text{ cm}^{-1}$, which is centered on the background adipose attenuation of 0.194 cm^{-1} so that non-uniformity in the background is easily seen.

T is constructed from the leading eigenvectors of $X^\top X$. The gain in convergence of the image RMSE metric by use of the low-rank preconditioner is shown in Fig. 7. Interestingly, using only the leading eigenvector by itself to form T results in a significant drop in image RMSE. Including additional eigenvectors does improve convergence, but the gain with each additional eigenvector becomes smaller and smaller. For the shown example, it is possible to reach the convergence rate of un-preconditioned CG by using 25 leading eigenvectors to form T . The low-rank preconditioner is also shown to be useful for the results from other configurations considered here.

3.4. Total-variation constrained least-squares convergence studies for full-sampling

In the following sub-sections, application of CPPD-TVCLSQ to reduced sampling configurations is presented. Here, we apply CPPD-TVCLSQ to the same full sampling system that is studied previously with CPPD-LSQ. For CPPD-TVCLSQ there are three algorithm parameters; as with CPPD-LSQ the iteration number and step-size ratio ρ need to be specified. Additionally, the TV constraint parameter, γ , must also be set for TVCLSQ problem. The present results focus on image recovery from ideal data, thus the constraint parameter is set to the phantom TV, i.e. $\gamma = \gamma_{\text{ph}}$.

As with CPPD-LSQ, 1000 iterations of CPPD-TVCLSQ are executed for several values of ρ . Shown in Fig. 8 are the curves corresponding to the ρ value that showed the most rapid convergence in the image RMSE. Note that the RMSE values reached are much lower than that of LSQ in Fig. 6 in particular the image RMSE convergence

is much more rapid for CPPD-TVCLSQ. Both the RMSE curves and the CPPD convergence metrics r_σ and r_τ show a rapid decreasing tend to zero, but then all curves hit a hard plateau. The source of the plateauing behavior has been traced to the finite precision of the computation, which is performed in single-precision floating point arithmetic. This has been verified by changing the computer variable precision from 4-byte to 8-byte floating point representation and by shrinking the overall size of the modelled tomographic system. There are ways to increase the numerical accuracy from fixed precision computation [19, 20], but we have not attempted this with the present CPPD-TVCLSQ implementation.

Applying the low-rank preconditioner in the form of a non-diagonal step matrix T is more complicated than the CPPD-LSQ case, because CPPD-TVCLSQ involves the stacking of two matrices X and D . In Appendix G one possible implementation of this preconditioner is presented for CPPD applied the TV-penalized least-squares. The same strategy also applies to CPPD-TVCLSQ, and the results of applying this preconditioner is shown in Fig. 9. As with CPPD-LSQ, the low-rank preconditioner improves the convergence rates seen in the image RMSE curves.

For inverse crime studies the CPPD convergence metrics r_σ and r_τ are not as directly meaningful as the image and data RMSE, but it is important to note the relative convergence between the RMSE curves and the CPPD convergence metrics

For inverse crime studies the CPPD convergence metrics r_σ and r_τ are not as directly meaningful as the image and data RMSE. It is, however, important to note the relative convergence between the RMSE curves and the CPPD convergence metrics, because the CPPD metrics will always tend to zero including the realistic conditions where the data contains inconsistencies, while the RMSE curves will in general not do so.

4. End of the main thread for now ...

The next two unlabelled subsections have results for sparse-view and limited angular range scanning. These results can be improved upon by optimizing the matrix stacking methodology. This topic will be added in a future version of these notes.

CPPD-TVCLSQ convergence studies, 32 projections over 2π scanning

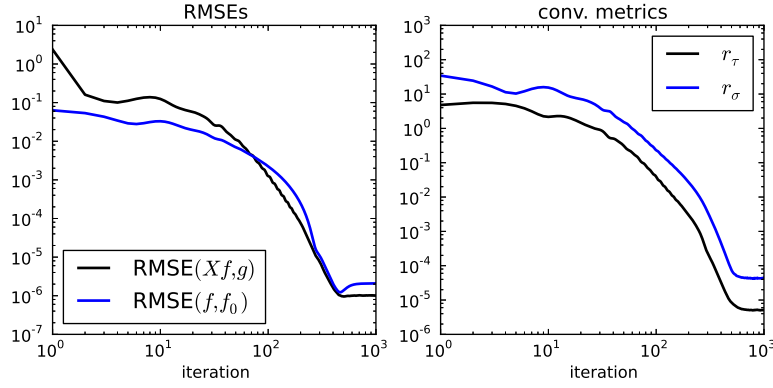


Figure 11. Convergence metrics for CPPD-TVCLSQ for a step-size ratio of $\rho = 0.2$. The left panel shows the image and data RMSE, and the right panel displays the transversality condition and splitting gap.

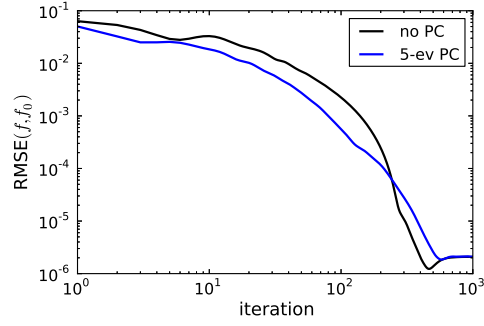


Figure 12. Impact of non-diagonal preconditioning (PC) on image RMSE for CPPD-TVCLSQ applied to image reconstruction for the 32-view data configuration. The legend indicates the number of eigenvectors (ev) of X used in forming the preconditioner. Also shown are the traces for scalar σ and τ , i.e. no preconditioning and generic CGLS.

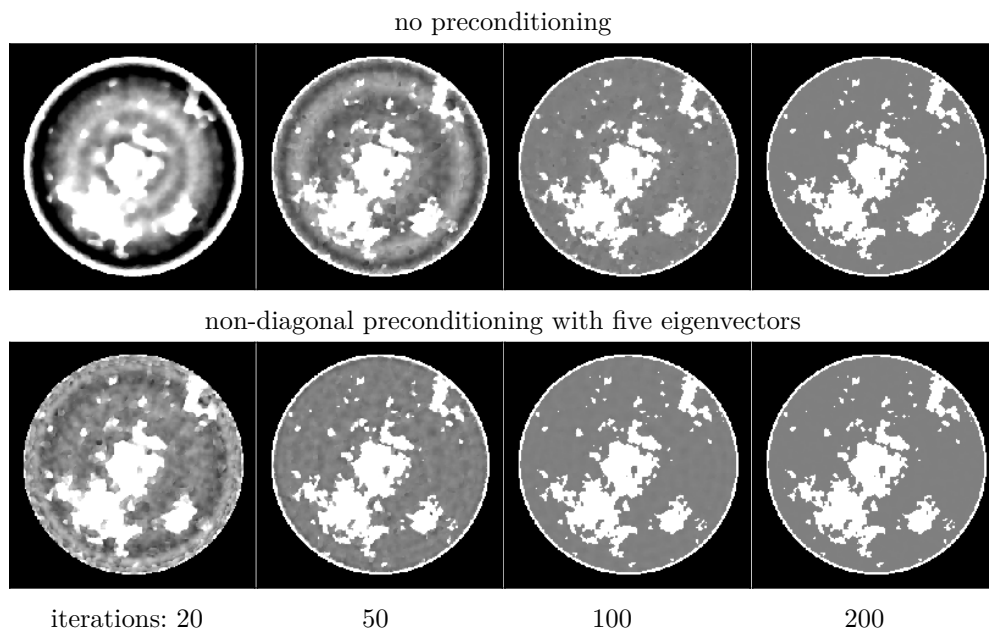


Figure 13. Sequence of image estimates for different iteration numbers of CPPD-TVCLSQ. Top row shows results for no preconditioning, and the bottom row displays images for non-diagonal preconditioning. The gray scale is $[0.174, 0.214]$ cm^{-1} , which is centered on the background adipose attenuation of 0.194 cm^{-1} so that non-uniformity in the background is easily seen.

CPPD-TVCLSQ convergence studies, 128 projections over $3\pi/4$ scanning

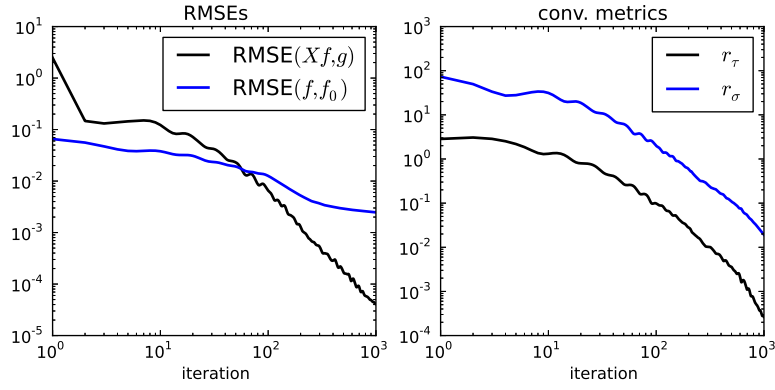


Figure 14. Convergence metrics for CPPD-TVCLSQ for a step-size ratio of $\rho = 0.5$. The left panel shows the image and data RMSE, and the right panel displays the transversality condition and splitting gap.

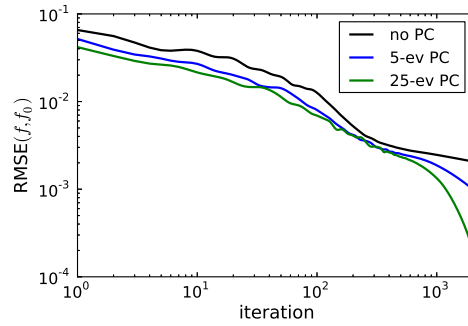


Figure 15. Impact of non-diagonal preconditioning (PC) on image RMSE for CPPD-TVCLSQ applied to image reconstruction for the 128-view, $3\pi/4$ angular range data configuration. The legend indicates the number of eigenvectors (ev) of X used in forming the preconditioner. Also shown are the traces for scalar σ and τ , i.e. no preconditioning and generic CGLS.

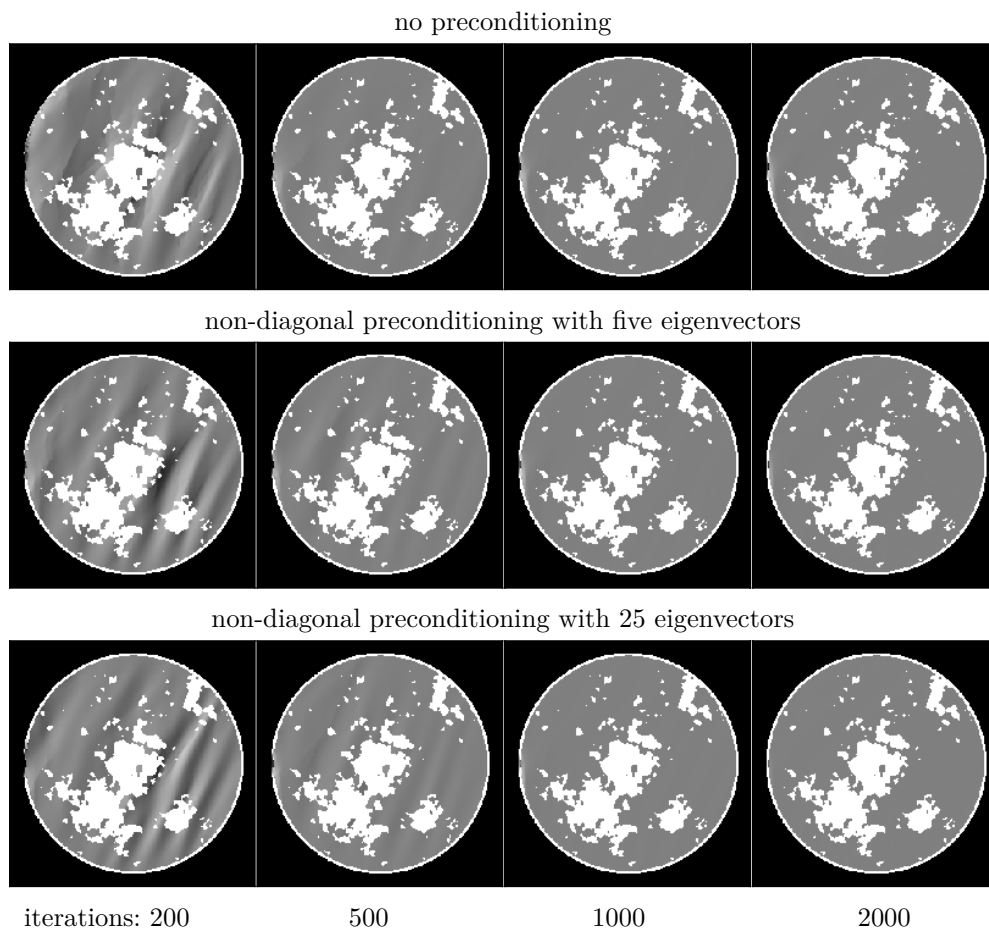


Figure 16. Sequence of image estimates for different iteration numbers of CPPD-TVCLSQ. Top row shows results for no preconditioning; the middle row displays images for 5-ev non-diagonal preconditioning; and the bottom row has the 25-ev results. The gray scale is $[0.174, 0.214] \text{ cm}^{-1}$, which is centered on the background adipose attenuation of 0.194 cm^{-1} so that non-uniformity in the background is easily seen.

Appendix A. Critical points and optimization

This appendix briefly summarizes the connection between critical points and optimization for smooth functions. For a function $f(x)$ the critical points occur at

$$\partial f(x_c) = 0.$$

Such points are related to extrema of $f(x)$, which can be specified by optimization: either minimization, maximization, or some combination thereof. All extrema of $f(x)$ are critical points, but not all critical points are extrema. We ignore, here, the complicating issue of local and global extrema. We need the connection between critical points and extrema for two reasons: (1) to write down the solution of an optimization problem as an equation; e.g. to be able to use

$$\partial f(x^*) = 0$$

as the solution of

$$x^* = \min_x f(x);$$

and (2) to go in the other direction, if we have a large-scale equation, where the solution can be viewed as a critical point of a potential, it can be helpful to write the problem as an optimization. The latter purpose is particularly useful when trying to develop iterative algorithms to solve an equation, as opposed to its direct solution.

To determine what type of extremum a critical point is or if it is an extremum at all, it is necessary to examine higher order derivatives. For example, for

$$f(x) = x^2,$$

$\partial f(x=0) = 0$, and $\partial^2 f(x=0) = 2$. Because the second derivative is positive we know that the critical point at $x_c = 0$ is a minimum, and this critical point can be specified by minimization

$$x_c = \min_x x^2.$$

Clearly, for

$$f(x) = -x^2,$$

$x_c = 0$ is a maximum because the second derivative is negative, and its critical point can be specified by maximization. But then there are more ambiguous situations such as

$$f(x) = x^3,$$

where the first and second derivatives are zero at $x_c = 0$. In this case, the lowest-order derivative, which is non-zero, is odd (namely the third-order derivative) so $x_c = 0$ is not an extremum and it cannot be specified by an optimization problem. The above examples apply no matter what is the dimension of x .

There is a type of extremum that is possible only if x is at least a 2-dimensional vector; namely a critical point in n -dimensions, $n \geq 2$, can be a saddle point - concave in some directions and convex in others. A clear example for 2-dimensional x is

$$f(x_1, x_2) = x_1^2 - x_2^2,$$

which is clearly convex as a function of x_1 and concave as a function of x_2 . Thus, this critical point can be specified by a combination of minimization and maximization

$$\min_{x_1} \max_{x_2} \{x_1^2 - x_2^2\}.$$

A less clear example, however, is

$$f(x_1, x_2) = x_1 x_2,$$

which is linear in x_1 and x_2 . Linear functions can be taken as convex or concave. To classify this critical point, we analyze it with second-order derivatives. The Hessian provides second-order characterization of multi-dimensional functions

$$\begin{aligned} H = \partial^2 f(x) &= \begin{pmatrix} \partial^2 f / \partial x_1^2 & \partial^2 f / \partial x_2 \partial x_1 \\ \partial^2 f / \partial x_1 \partial x_2 & \partial^2 f / \partial x_2^2 \end{pmatrix} \\ &= \begin{pmatrix} 0 & 1 \\ 1 & 0 \end{pmatrix}. \end{aligned}$$

The critical point classification can then be determined by diagonalization of H . The eigenvalues of H yield the curvature of f in the directions of the eigenvectors. If there are negative and positive eigenvalues of H , the critical point is a saddle point. In this particular example, the eigenvalues are 1 and -1 corresponding to the eigenvectors $(1, 1)^\top$ and $(1, -1)^\top$, respectively. Thus, we know that $f(x) = x_1 x_2$ is a saddle point. Changing coordinates as suggested by the diagonalization

$$\begin{aligned} s &= x_1 + x_2, \\ t &= x_1 - x_2, \end{aligned}$$

makes this abundantly clear

$$x_1 x_2 = (s^2 - t^2)/4.$$

We know that optimization of $f(x) = x_1 x_2$ to find the critical point involves min-max because the critical point is a saddle point. Interestingly, this critical point can be specified by either of the following min-max problems

$$\begin{aligned} \min_{x_1} \max_{x_2} x_1 x_2, \\ \min_{x_2} \max_{x_1} x_1 x_2, \end{aligned}$$

where actually being able to carry out the calculation of these min-max problems requires non-smooth analysis and this is discussed in Appendix B.

Analyzing the only the bilinear term in the saddle-point optimizations in Eqs. (2) and (6) the stationary saddle-point can be identified in two ways. For the bilinear term in Eq. (2), if maximization is selected for the variables x and y , minimization must be performed over λ . If minimization is chosen for x and y , maximization must be selected for λ . The reason why minimization over x and y is used when considering the complete Lagrangian expression in Eq. (2) is that $\phi(y)$ is convex. Likewise, for Eq. (6), maximization over λ is selected because $-\phi^*(\lambda)$ is concave.

Appendix B. Non-smooth convex functions

The workings of the Chambolle-Pock primal-dual (CPPD) algorithm can be mostly understood within the context of smooth optimization, but one of the main

motivations for using the CPPD algorithm is to perform optimization with non-smooth convex functions. Accordingly, we do need to cover this topic, but we attempt to do so with a bare minimum of material. For more in depth presentation, the reader is referred to the classic text by Rockafellar [2]. There are also a number of other textbooks, e.g. [21], tutorial papers, and online reference material on this topic. The approach to the presentation here is greatly simplified by a comment made by Marc Teboulle, co-author of FISTA [22], at the 2014 SIAM Imaging Science conference in Hong Kong. In the discussion after a presented paper on non-smooth optimization, Marc pointed out that in dealing with non-smooth convex optimization the vast majority of cases where it is used center on the absolute value and the indicator functions. The absolute value function is well-known, but the indicator function might be less familiar to a medical physics audience.

Indicator functions are a convenient construct in convex analysis for converting a convex set into a convex function

$$\delta_C(x) = \begin{cases} 0 & x \in C \\ \infty & x \notin C \end{cases},$$

where C is a convex set. Clearly, the absolute value and indicator functions are not differentiable everywhere. The concept of differentiation can be generalized to accommodate non-smoothness, and this topic is taken up in Appendix D.

For optimization, the indicator function allows the restriction of possible solutions to various convex constraints by adding infinite walls to the objective function. In performing addition of convex functions, we need an additional rule for handling infinity

$$a + \infty = \infty, \tag{B.1}$$

where a is any scalar, and for $a > 0$

$$a \cdot \infty = \infty, \tag{B.2}$$

and

$$0 \cdot \infty = 0. \tag{B.3}$$

Using the algebra of convex functions, constrained optimization can be made to look like unconstrained optimization.

For example, the convex constrained minimization problem

$$\min_x \frac{1}{2}x^2 \text{ such that } 1 \leq x \leq 2$$

can be written as the convex minimization

$$\min_x \left\{ \frac{1}{2}x^2 + \delta_S(x) \right\} \text{ where } S = \{x | x \in [1, 2]\},$$

using Eq. (B.1).

We are now in a position to analyze the saddle-point optimization

$$\min_{x_1} \max_{x_2} x_1 x_2.$$

Performing the maximization over x_2 first

$$\max_{x_2} x_1 x_2,$$

three cases need to be considered: $x_1 < 0$, $x_1 = 0$, and $x_1 > 0$. For $x_1 < 0$, the maximizer is $x_2 = -\infty$ and the maximum for this case is ∞ . For $x_1 = 0$, the maximum for this case is 0. For $x_1 > 0$, the maximizer is $x_2 = \infty$ and the maximum is ∞ . Putting these cases together, we have

$$\max_{x_2} x_1 x_2 = \delta_Z(x_1) \text{ where } Z = \{0\}.$$

Minimization over $\delta_Z(x_1)$ is trivial; the minimizer is $x_1 = 0$. Thus the saddle-point is identified to be $x_1 = x_2 = 0$. Note that in performing this saddle-point optimization it is necessary to use the rules for multiplication with ∞ .

Appendix C. The Legendre-Fenchel transform

The Legendre-Fenchel (LF) transform, also known as convex conjugation, is one of the main operations in convex analysis. It essentially provides a way to represent a convex function in terms of linear functions that support its epigraph. For scalar functions of a vector, this concept generalizes straight-forwardly to planar support functions. It is useful for manipulating and simplifying optimization problems when the order of optimization operations can be interchanged. In such cases minimization/maximization can be performed on the component lines instead of the function itself. This capability with convex analysis is analogous to Fourier analysis, where functions are decomposed in plane waves and integration/differentiation operations can be performed on the individual plane wave components. See Table 1 of Ref. [23] for a more complete comparison of Fourier and convex analysis. In the following, we present the discussion in terms of a convex function $f(x)$ in 2D, i.e. x is a scalar, and occasionally insert remarks on generalizing x to a vector. All formulas, however, are written so that they apply to the multi-dimensional vector case.

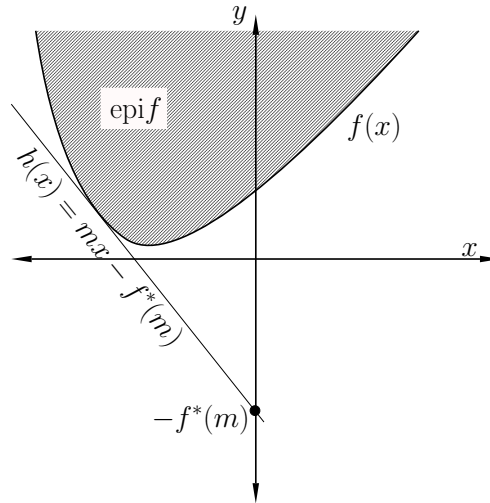


Figure C1. Schematic of a convex function $f(x)$ and its epigraph. The indicated line satisfies $h(x^*) = f(x^*)$ and $h(x) \leq f(x)$. The line $h(x)$ intercepts the y -axis at $-f^*(m)$.

The LF transform essentially yields a parameterization of the epigraph supporting lines in terms of their slope. The convex function $f(x)$ can be represented as the max

over all lines that lie below $f(x)$. Parameterizing such a line by a slope m and “ y -intercept” $-b$ (in the multi-dimensional case, m is a vector of the same dimension as x , and b is still a scalar)

$$h(x) = m^\top x - b, \quad (\text{C.1})$$

the constraint that $h(x)$ lies below $f(x)$ is enforced by constraining b to satisfy

$$b \geq m^\top x - f(x). \quad (\text{C.2})$$

The set of m and b that specify lines that satisfy this inequality are denoted by the set F^*

$$(m, b) \in F^*,$$

if Eq. (C.1) holds for all x . We then can write the function $f(x)$ as a maximization

$$f(x) = \max_{(b,m) \in F^*} \{m^\top x - b\}. \quad (\text{C.3})$$

This representation of $f(x)$ can be reduced to just the supporting lines, i.e. the lines that actually intersect $f(x)$ at at least one point, by restricting b to the smallest possible value for a given slope m .

$$\begin{aligned} b &\geq m^\top x - f(x), \\ b &\geq \max_x \{m^\top x - f(x)\}, \\ b_{\min}(m) &= \max_x \{m^\top x - f(x)\}. \end{aligned}$$

The LF transform of $f(x)$, $f^*(m)$, is defined to be $b_{\min}(m)$, i.e.

$$f^*(m) = \max_x \{m^\top x - f(x)\}, \quad (\text{C.4})$$

and by construction F^* is the epigraph of $f^*(m)$. The LF transform has a clear geometric meaning, shown in Fig. C1, which can be exploited to compute transforms of specific functions in addition to analysis techniques.

Because F^* is the epigraph of $f^*(m)$, we can perform the maximization over b in Eq. (C.3) yielding

$$f(x) = \max_m \{m^\top x - f^*(m)\}. \quad (\text{C.5})$$

Comparing Eqs. (C.4) and (C.5), we see that the LF transform is its own inverse, and

$$f^{**} = f,$$

provided that f and f^* are convex. Because of this relation the LF transform is often referred to as convex conjugation. If f is not convex, we can not write Eq. (C.3) and Eq. (C.5) does not hold. Whether or not f is convex, we can still compute its LF transform f^* with Eq. (C.4) and in doing so, f^* will be convex. Also, if f is non-convex, f^{**} is the tightest convexification of f .

We present the argument that $f^*(m)$ is convex, if it is computed from Eq. (C.4). Considering the points $(x, z) \in F$, where F is the epigraph of $f(x)$, the maximization in Eq. (C.4) can be written

$$f^*(m) = \max_{(x,z) \in F} \{m^\top x - z\}, \quad (\text{C.6})$$

where we have used the fact that point (x, z) lies above $(x, f(x))$. Thus, we see that $f^*(m)$ is a maximization over lines in m -space

$$g(m) = x^\top m - z,$$

where x plays the role of a slope and $-z$ is the corresponding y -intercept. Because $f^*(m)$ is a maximization over convex functions it is itself convex.

Nevertheless, even if f is non-convex, f^* is convex because Eq. (C.6) still holds and in this case f^{**} is the tightest convexification of f . Because $f^{**} = f$ for convex functions, the LF transform is often referred to as convex conjugation.

Appendix C.1. LF transform examples

In order to illustrate the main approaches to computing the LF transform, we find f^* for quadratic, absolute value, linear, and indicator functions.

(I) $f(x) = ax^2/2$: For a differentiable convex function one can use the standard optimization technique of setting the gradient of the objective function to zero, solving for the maximizer, and then plugging the maximizer back into the objective function to obtain the function max. Starting from Eq. (C.4), we differentiate the objective function with respect to x and set to 0

$$\partial f(x^*) = m,$$

where x^* denotes the maximizer of Eq. (C.4), i.e. the value of x where the slope of $f(x)$ is m . For the quadratic example, we have

$$\begin{aligned} ax^* &= m, \\ x^* &= m/a. \end{aligned}$$

We plug this back into the LF objective function

$$f^*(m) = m^\top x^* - f(x^*) = m^2/(2a),$$

obtaining another quadratic, with inverse width, as a now appears in the denominator. This example also hints at the duality nature of the LF transform; as an exercise it is worthwhile to show that applying the LF transform again will yield a quadratic with a back in the numerator – the same function we started with.

The multi-dimensional case is a trivial extension, because the LF objective function separates. Generalizing the one-dimensional quadratic, we have

$$f(x) = x^\top Ax/2,$$

where $A = \text{diag}(a)$ is a diagonal matrix with all positive diagonal elements $a > 0$. The LF transform is

$$\begin{aligned} f^*(m) &= \max_x \{m^\top x - x^\top Ax/2\}, \\ &= \sum_i \max_{x_i} \{m_i x_i - a_i x_i^2\}, \\ &= \sum_i m_i^2/(2a_i), \\ &= m^\top A' m/2, \end{aligned}$$

where $A' = \text{diag}(1/a)$.

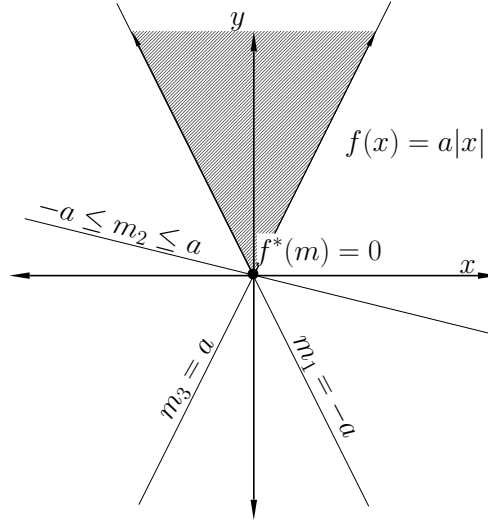


Figure C2. Schematic of a convex function $f(x) = a|x|$ and its LF transform. Three support lines for this function are indicated. The lines labelled m_1 , m_2 , and m_3 are respectively the lines with lowest possible slope, a generic support line, and the line with highest possible slope. All support lines intersect the y -axis at 0; hence the LF transform is zero for the allowed slopes $-a \leq m \leq a$.

(II) $f(x) = a|x|$: The LF transform of the absolute value can be handled analytically, considering the cases where the minimizer is positive or negative. There is, however, a much simpler geometric approach using Fig. C1, which we adapt to the function of interest in Fig. C2. From this figure, the support lines to $a|x|$ all have slope between $-a$ and a , and the y -intercept of all the supporting lines is 0, hence

$$f^*(m) = \delta(-a \leq m \leq a).$$

The use of the indicator allows us to restrict the domain of slopes to those of the support lines, and when the slope is between $-a$ and a the indicator's value is zero.

For the multi-dimensional generalization, we consider

$$f(x) = a\|x\|_1,$$

where a in this case is still a scalar. It is possible to employ the purely geometric approach, but it is simpler to take advantage of the separable objective function

$$\begin{aligned} f^*(m) &= \max_x \{m^\top x - \|x\|_1\}, \\ &= \sum_i \max_{x_i} \{m_i x_i - a|x_i|\}, \\ &= \sum_i \delta(-a \leq m_i \leq a), \\ &= \delta(\|m\|_\infty \leq a), \end{aligned}$$

where $\|\cdot\|_\infty$ yields the magnitude of the largest component of its argument

$$\|m\|_\infty = \max(|m|_1, |m|_2, \dots, |m|_i, \dots).$$

In summary, the ℓ_1 norm LF transform is most easily dealt with by a combination of geometric and analytic methods; the LF optimization problem is separated analytically and the individual one-dimensional optimization problems are handled geometrically.

(III) $f(x) = ax + c$: Using the geometric approach for a linear function is also quite straight-forward. There is only one support line with slope $m = a$. From Fig. C1 the value of f^* is the negative y -intercept, and the y -intercept for the line of interest is c . As a result, f^* for $m = a$ has the value of $-c$

$$f^*(m) = \delta(m = a) - c.$$

The indicator function reduces the domain of the function to a single point in this case, and subtracting c does not alter this because of Eq. (B.1). This same argument and formula applies for the multi-dimensional case of $f(x) = a^\top x + c$.

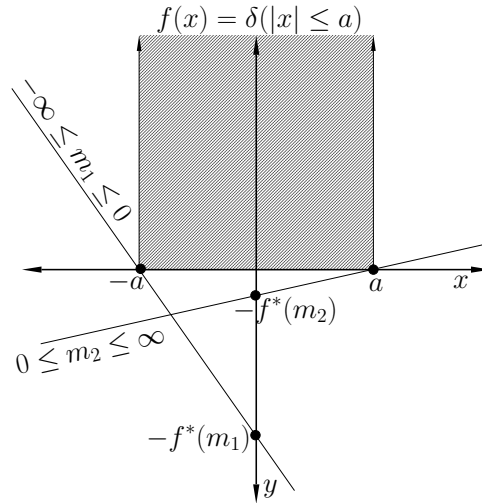


Figure C3. Schematic of a convex function $f(x) = \text{delta}(|x| \leq a)$ and its LF transform. Two support lines for this function are indicated. The lines labelled m_1 and m_2 are the generic support lines that intersect $f(x)$ at $x = -a$ and $x = a$, respectively. Note that one support line with $m = 0$ intersects $f(x)$ over the whole segment between $x = -a$ and $x = a$. Also shown are the y -intercepts for the lines m_1 and m_2 . By geometric reasoning it is clear that $f^*(m_1) = -am_1$ and $f^*(m_2) = am_2$. Putting these cases together yields the result $f^*(m) = a|m|$.

(IV) indicator functions $f(x) = \delta(-a \leq x \leq a)$ and $f(x) = \delta(x = a) - c$: For the indicator function examples we choose exactly the same functions we arrived at from the previous two examples of LF transforms. In both cases it is simplest to use the geometric approach. For

$$f(x) = \delta(-a \leq x \leq a),$$

we see in Fig. C3 that lines of all slopes m contribute to the function support and the desired LF transform can be extracted from the negative y -intercept of the drawn lines. We thus obtain

$$f^*(m) = a|m|.$$

For

$$f(x) = \delta(x = a) - c,$$

the same approach yields its LF transform

$$f^*(m) = am + c.$$

In both cases we observe that the LF transform has inverted the previous two examples.

Appendix D. The subdifferential and subgradient

For convex functions the subdifferential is a useful generalization of standard differentiation of smooth functions. The subdifferential $\partial f(x)$ is a set-valued mapping defined by the following inequality

$$\partial f(x) = \{m \mid \forall x' : f(x') \geq f(x) + m^\top(x' - x)\}. \quad (\text{D.1})$$

For functions of a scalar, the subdifferential at any point x is the set of slopes of lines that pass through $f(x)$ but lie completely underneath $f(x)$. Equation (D.1) expresses the n -dimensional generalization of this idea. For differentiable $f(x)$, $\partial f(x)$ yields the usual gradient. A sub-gradient g is one of the elements of $\partial f(x)$

$$g \in \partial f(x).$$

The subdifferential is useful for convex functions because there will always be at least one linear function that goes through $f(x)$ and lies completely beneath $f(x)$. Also, in this paper we are primarily concerned with first-order algorithms and optimality conditions, and first-order subdifferentiation is uncomplicated.

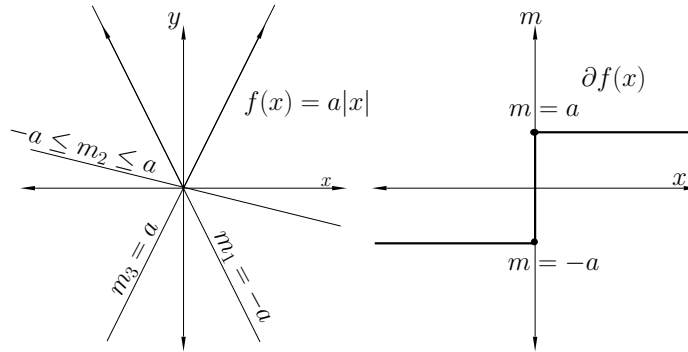


Figure D1. Schematic of a convex function $f(x) = a|x|$ (left) and its subdifferential (right). The lines indicated by the slope m_1 , m_2 , and m_3 yield the subdifferential for $x < 0$, $x = 0$, and $x > 0$, respectively. For $x \neq 0$ this function is smooth, and accordingly the subdifferential is the standard gradient. For $x = 0$, lines with slope $|m_2| \leq a$ all fit underneath the function while intersecting $f(0) = 0$. Thus for this point the subdifferential is the set $[-a, a]$.

The classic example illustrating the subdifferential for a non-smooth function is $\partial f(x)$ when

$$f(x) = a|x|.$$

This function and its subdifferential are illustrated in Fig. D1. The subdifferential is multi-valued only at $x = 0$ where the function is not-differentiable. In particular, we note that the subgradient $g = 0$ is a member of the subdifferential $\partial f(x = 0)$ and at the same time $x = 0$ is the minimum of this function. In fact, the first-order condition of optimality for a convex, non-smooth function is

$$0 \in \partial f(x^*),$$

which is the generalization of the condition

$$0 = \partial f(x^*),$$

for differentiable f . We note also that a minimum at a non-smooth point lends robustness to the minimizer; i.e. perturbing the function by a smooth function will not change the minimizer unless the slope of the perturbation exceeds the extreme values of the subdifferential at the minimizer.

In the main text, the subdifferential concept is not absolutely necessary for the development. For non-smooth F or F^* , ∂F and ∂F^* can be multivalued in these equations. Also, the maximizer in the LF transform objective function is specified by the subdifferential. This is seen in the similarity between Figs. C2 and the left-hand graph in D1. While we do not absolutely need the concept of the subdifferential to compute the LF transform as we saw in Appendix C, we can now express the maximizer of the LF objective function in Eq. (C.4) formally as x^* satisfying the equation

$$m \in \partial f(x^*).$$

Appendix E. Saddle point solver intuition

Saddle point optimization is fundamentally different than convex function minimization or concave function maximization. A saddle potential has at least one direction of negative curvature and one direction of positive curvature, and accordingly the minimum dimension for saddle point optimization is two, while both minimization and maximization can be performed for functions of scalars. As a result, the intuition for saddle point optimization is more complex than that of minimization/maximization. Specifically, for the latter one can imagine computing the function gradient and taking a step in that direction for maximization or in the opposite direction for minimization. For saddle point optimization, using only first-order or gradient information, an algorithm needs to go uphill, with the gradient, for variables that are being maximized over and downhill, against the gradient, for variables that are being minimized over. While the decomposition of the gradient to form a step-direction for a saddle point optimization algorithm seems straightforward, complications arise when the coordinates are not well aligned with the directions of curvature, and this is the reason why the CPPD algorithm is significantly more complex than basic gradient descent/ascent for minimization/maximization.

In this appendix, we present examples of saddle point optimization that serve to motivate the particular form of the CPPD update steps and to illustrate convergence behavior as a function of algorithm parameters. This appendix contains examples of forward Euler iteration that gives a more complete picture of its behavior with saddle point problems; a couple examples of the approximate backward Euler iteration then motivate the particular choice of CPPD algorithm parameter settings; and then finally the convergence behavior of the CPPD applied to least-squares minimization is explained by use of an eigenvector decomposition.

Appendix E.1. Saddle point optimization with forward Euler iteration

As discussed in Sec. 2.2.1 the forward Euler iteration for finding the saddle point of

$$s(x, \lambda) = \lambda^\top A x$$

does not converge for any step size. Recall that the forward Euler iteration for this problem is

$$\begin{aligned} x_{k+1} &= x_k - \alpha A^\top \lambda_k \\ \lambda_{k+1} &= \lambda_k + \alpha A x_k, \end{aligned}$$

where k is the index number for the iteration. The simplest special case of this problem occurs when both x and λ are scalars and $A = 1$

$$s_0(x, \lambda) = \lambda x,$$

and the corresponding forward Euler iteration is

$$\begin{aligned} x_{k+1} &= x_k - \alpha \lambda_k \\ \lambda_{k+1} &= \lambda_k + \alpha x_k. \end{aligned}$$

The saddle point of $s_0(x, \lambda)$ is at $x = \lambda = 0$, but if the forward Euler iteration is initialized away from this saddle point, the subsequent iterations will spiral away from the origin of $x\lambda$ -plane. If the current iterate is x_k, λ_k , its distance from the origin is

$$r_k = \sqrt{x_k^2 + \lambda_k^2}.$$

Using the update equations, one can show that the distance of the next iterate is related to the current distance by

$$r_{k+1} = \sqrt{1 + \alpha^2} r_k.$$

Clearly, the distance of the iterates from the origin will increase for any value of the step size parameter α . This example, however, does not mean that forward Euler iteration always fails to converge for saddle point problems.

Consider a different potential

$$s_1(x, \lambda) = x^2 - \lambda^2,$$

where x and λ are scalars. This potential also has a critical point at $x = \lambda = 0$, which is a saddle point. In this case the forward Euler updates, derived by a taking a step in the direction of the derivative of λ and opposite to the direction of the derivative in x , are

$$\begin{aligned} x_{k+1} &= x_k - 2\alpha x_k = (1 - 2\alpha)x_k \\ \lambda_{k+1} &= \lambda_k - 2\alpha \lambda_k = (1 - 2\alpha)\lambda_k. \end{aligned}$$

By inspection, it is clear that the relationship between successive distances to the origin for these update formulas is

$$r_{k+1} = (1 - 2\alpha)r_k,$$

and the choice of $0 < \alpha < 1$ leads to convergence to the saddle point at the origin of the $x\lambda$ -plane. Interestingly, the potentials s_0 and s_1 are related by rotation of 45 degrees; i.e. the variable substitution $x' = x + \lambda$ and $\lambda' = x - \lambda$ turns one of these potentials into the other, up to a scalar multiple.

The fact that s_0 and s_1 are related by simple rotation would seem to suggest a possible means to attack the general saddle point problem

$$\min_x \max_\lambda \{ \lambda^\top A x - \phi^*(\lambda) \},$$

where maybe a coordinate change would allow forward Euler iteration to be successfully applied. The barrier to this strategy is that the equivalent to performing the rotation of s_0 to s_1 involves second-order information, namely computing the eigendecomposition of the Hessian of this saddle potential. This can be prohibitively expensive for large-scale optimization.

Fortunately, there is a way to address the saddle point optimization problem of interest using only first order information as given by the approximate backward Euler iteration in Sec. 2.2.3. As there are a number of parameters in the original form of this algorithm, it is illustrative to examine it in the special case saddle point potentials $s_0(x, \lambda)$ and another one corresponding to one-dimensional quadratic optimization.

Appendix E.2. Saddle point optimization with approximate backward Euler iteration

Recall from Sec. 2.2.3 that the approximate backward Euler step can optimize the saddle potential $s(x, \lambda)$, and the update steps given in Eqs. (15)-(17) are repeated here

$$\begin{aligned} x_{k+1} &= x_k - \tau A^\top \lambda_k, \\ \bar{x}_{k+1} &= x_{k+1} + \theta(x_{k+1} - x_k), \\ \lambda_{k+1} &= \lambda_k + \sigma A \bar{x}_{k+1}. \end{aligned}$$

There are three algorithm parameters σ , τ , and θ . According to Ref. [1], these parameters should be chosen, respecting the following inequalities

$$0 \leq \theta \leq 1, \quad \sigma\tau < \|A\|_2,$$

where the latter strict inequality can be taken as \geq in most cases of practical interest.

Applying this algorithm to the two-dimensional saddle point problem $s_0(x, \lambda)$, $A = 1$ and the update steps reduce to

$$\begin{aligned} x_{k+1} &= x_k - \tau \lambda_k, \\ \lambda_{k+1} &= \lambda_k + \sigma((1 + \theta)x_{k+1} - \theta x_k), \end{aligned}$$

where the extrapolation step is absorbed into the λ update. Parameterizing the step-lengths in terms of their product a and allowing the equality case for this product, τ can be written in terms of σ and a

$$\sigma\tau = a \leq 1.$$

The update steps can thus be manipulated into the following matrix-vector product form

$$\begin{pmatrix} x_{k+1} \\ \lambda_{k+1} \end{pmatrix} = \begin{pmatrix} 1 & -a/\sigma \\ \sigma & 1 - a - \theta a \end{pmatrix} \begin{pmatrix} x_k \\ \lambda_k \end{pmatrix}.$$

Considering a couple of special cases provides some orientation on the parameter dependences of the iteration with this update.

$\theta = 1$ and $a = 1$: These parameter settings yield

$$\begin{pmatrix} x_{k+1} \\ \lambda_{k+1} \end{pmatrix} = \begin{pmatrix} 1 & -1/\sigma \\ \sigma & -1 \end{pmatrix} \begin{pmatrix} x_k \\ \lambda_k \end{pmatrix},$$

and it is straight-forward to verify that

$$\begin{pmatrix} x_{k+2} \\ \lambda_{k+2} \end{pmatrix} = \begin{pmatrix} 0 & 0 \\ 0 & 0 \end{pmatrix} \begin{pmatrix} x_k \\ \lambda_k \end{pmatrix}.$$

This result means that no matter what x_0 and λ_0 are initialized to, the updates will converge in two steps to the saddle point at $(x, \lambda) = (0, 0)$, independent of σ .

$\theta = 0$ and $a = 1$: These parameter settings yield

$$\begin{pmatrix} x_{k+1} \\ \lambda_{k+1} \end{pmatrix} = \begin{pmatrix} 1 & -1/\sigma \\ \sigma & 0 \end{pmatrix} \begin{pmatrix} x_k \\ \lambda_k \end{pmatrix}.$$

From this update, one can show that

$$\begin{pmatrix} x_{k+8} \\ \lambda_{k+8} \end{pmatrix} = \begin{pmatrix} 1 & 0 \\ 0 & 1 \end{pmatrix} \begin{pmatrix} x_k \\ \lambda_k \end{pmatrix},$$

and it is clear that the updates will repeat values every eighth iteration and not converge to the saddle point, again, independent of σ 's value. Thus, we encounter a case where the step-size product must respect the strict inequality $a < 1$ in order to converge.

These two specific cases provide a heuristic for selecting $\theta = 1$, but this particular saddlepoint problem is too simple to provide intuition on why it is important to tune the step-size ratio

$$\rho = \sqrt{\sigma/\tau}.$$

No matter what value is chosen for σ , the two particular parameter settings shown yield the same results.

Appendix E.3. Tuning the step-size ratio of the CPPD algorithm

In order to appreciate the impact of the step-size ratio in the CPPD algorithm the minimum complexity problem to consider is one-dimensional quadratic optimization. Specifically, consider the minimization

$$\min \frac{1}{2} x^2.$$

Repeating the steps described in Sec. 2.1, allows this minimization to be generalized to the saddle point problem

$$\min_x \max_\lambda \left\{ x\lambda - \frac{1}{2}\lambda^2 \right\},$$

which is a special case of Eq. (6). The solution for the minimization is clearly $x = 0$ and the saddle point for the second potential is $(x, \lambda) = (0, 0)$. The approximate backward Euler iteration for this saddle potential is

$$\begin{pmatrix} x_{k+1} \\ \lambda_{k+1} \end{pmatrix} = \begin{pmatrix} 1 & \frac{-a}{\sigma} \\ \frac{\sigma}{1+\sigma} & \frac{1-\sigma a}{1+\sigma} \end{pmatrix} \begin{pmatrix} x_k \\ \lambda_k \end{pmatrix},$$

where $\theta = 1$, $\sigma\tau = a$, and $a \leq 1$. Fixing a and varying σ effectively varies the step-size ratio ρ . Even with θ set to one this update step is complicated to analyze with analytic methods; a given update trajectory depends non-trivially on the initial values (x_0, λ_0) , a , and σ . For comparison, consider the gradient descent (GD) update for the corresponding quadratic minimization

$$x_{k+1} = x_k - ax_k = (1 - a)x_k,$$

where convergence is attained for $0 < a < 2$ and any iterate can be computed directly from the initial value by

$$x_k = (1 - a)^k x_0.$$

The trajectory of the iterates x_k is clearly easier to characterize than the trajectory of x_k, λ_k for the CPPD algorithm.

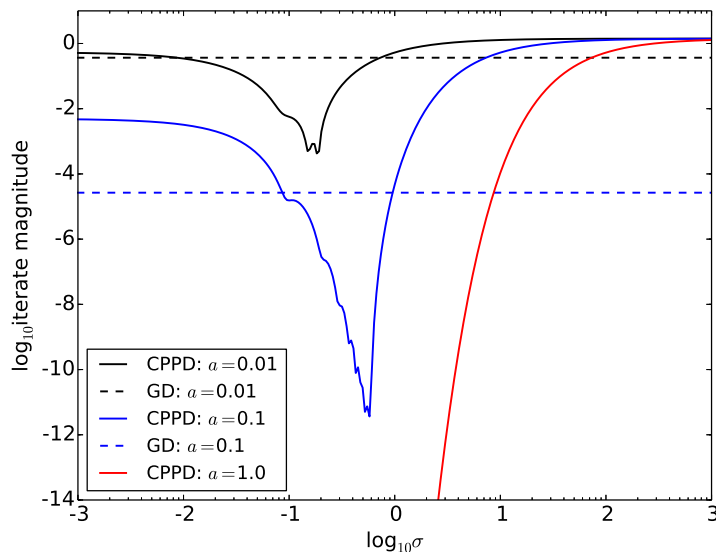


Figure E1. Plotted is the magnitude of (x_k, λ_k) after 100 iterations. The initial values are $(x_0, \lambda_0) = (1, 0)$; σ is varied from 10^{-3} to 10^3 ; and curves are shown for $a = 0.01$, $a = 0.1$, and $a = 1.0$. For comparison, the gradient descent (GD) iterate magnitude $|x_k|$ after 100 iterations for the corresponding a values. Note that GD does not depend on σ . Also, GD is not shown for $a = 1$, because convergence is obtained in one iteration for this case.

A specific case is shown in Fig. E1 for one set of initial values, where the magnitude of the iterate vector (x_k, λ_k) is shown after 100 iterations and compared with the GD algorithm. The iterate magnitude is an indication of convergence, because the solution to the quadratic minimization and saddle point problem is 0 and $(0, 0)$, respectively. For the case of $a = 1$, CPPD converges rapidly for small σ , but GD converges in one iteration. For $a = 0.1$, there is a clear minimum in the iterate magnitude at $\sigma \approx 0.5$ and that magnitude is much smaller than what is attained by GD. Similarly for $a = 0.01$, there is a minimum at $\sigma \approx 0.2$, which is much smaller than the corresponding GD result. For $a = 1$, GD outperforms CPPD in terms of convergence since it converges in one iteration. But for the other a values, CPPD outperforms GD provided that σ is tuned. If the σ parameter is not tuned, the CPPD iterations can converge very slowly, even more slowly than GD.

This example is actually relevant to large-scale least-squares optimization. Performing an SVD of the system matrix leads to a set of uncoupled one-dimensional quadratic optimizations. In such a decomposition and normalizing the system matrix to 1, the parameter a takes on the role of the eigenvalues of the system matrix. Performing the CPPD iteration for the least-squares system is equivalent to selecting the same σ value for all of the one-dimensional quadratic sub-problems obtained by the SVD analysis. For example, the plot in Fig. E1 is useful for analyzing a system matrix with only three eigenvectors with eigenvalues 0.01, 0.1, and 1.0. In this case, we note that the $a = 0.01$ curve is the largest for all shown σ values; σ should be chosen by finding the minimum of this curve.

This analysis, however, is only for illustrative purposes. The CPPD trajectory has a lot of complexity not captured by Fig. E1. Furthermore, SVD of large-scale system matrices may not be practical. In practice, it is simpler to directly tune σ or equivalently the step-size ratio ρ , for fixed $\sigma\tau$.

Appendix F. Fixed-point iteration, the proximal point algorithm, resolvents, and monotone operators

To provide further insight into the CPPD algorithm, we summarize the fixed-point iteration formalism in which convergence of this and other recent first-order algorithms can be readily shown. In this appendix, fixed-point iteration is explained with a couple of one-dimensional examples. First, the familiar gradient descent algorithm is cast as a fixed-point iteration in order to obtain intuition on how fixed-point iteration relates to optimization. Second, a specific form of fixed-point iteration called the proximal point algorithm is presented in order to appreciate its effectiveness with non-smooth optimization. Finally, the generalization of the proximal point algorithm to the CPPD and other related algorithms requires the concept of the resolvent and monotone operators, which are briefly explained here. For further reading on how the CPPD can be framed as a generalized proximal point algorithm, please consult the article by He and Yuan [6]. An excellent tutorial paper on fixed-point iteration by Ryu and Boyd [24] explains a number of recent first-order algorithms, including ADMM, ISTA, Douglas-Rachford, and CPPD.

A fixed point, x^* , of an operator M obeys the equation

$$x^* = M(x^*).$$

An algorithm for finding such points is the fixed-point algorithm

$$x^{(k+1)} = M(x^{(k)}),$$

where an initial guess $x^{(0)}$ is made and subsequent iterations indexed by k are obtained by feeding the output of M back into M . Convergence of this algorithm to x^* is discussed after showing gradient descent and proximal point examples.

Appendix F.1. Gradient descent as fixed-point iteration

The gradient descent algorithm to find a minimizer x^* of a smooth convex function $f(x)$, involves making an initial guess $x^{(0)}$ and performing the following iteration

$$x^{(k+1)} = x^{(k)} - \alpha \nabla f(x^{(k)}), \tag{F.1}$$

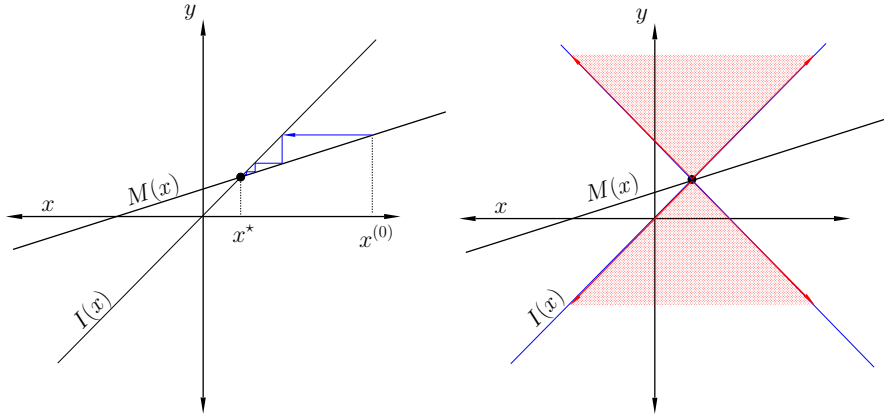


Figure F1. Left: Schematic of fixed-point iteration corresponding to gradient descent of a quadratic function $f(x) = (1/2)(x - x^*)^2$. The fixed-point operator is $M(x) = (I - \alpha \nabla f)(x) = (1 - \alpha)x + \alpha x^*$. Graphically, fixed-point iteration starts at $M(x_0)$ and alternates between horizontal projection onto $I(x)$ and vertical projection onto $M(x)$. This iteration converges to the minimizer x^* , where M and I intersect, if α is chosen appropriately. Right: Diagram indicating region where fixed-point iteration with $M(x)$ converges to x^* . Consider the following cases: $\alpha < 0$, $M(x)$ is in the red zone because it has a slope greater than 1 and fixed-point iteration will diverge; $\alpha = 0$, M and I coincide and all iterates equal x_0 ; $0 < \alpha < 1$, iterations approach solution from one side; $\alpha = 1$, M is horizontal and convergence to x^* is achieved in one iteration; $1 < \alpha < 2$, iterates approach x^* but are under-relaxed as successive iterates are on opposite sides of x^* ; $\alpha = 2$ iterates oscillate between x_0 and $-x_0$; and finally $\alpha > 2$, M is once again in the red zone and fixed-point iteration diverges.

where for each estimate $x^{(k)}$ the gradient descent step involves subtracting a step length parameter α times the gradient at that estimate. In fixed-point operator form, this iteration is written

$$x^{(k+1)} = M(x^{(k)}), \quad M(x) = (I - \alpha \nabla f)(x),$$

where I is the identity operator. At the minimizer x^* , the gradient of f is zero and hence $x^* = M(x^*)$. Whether or not an arbitrary initial guess will converge toward x^* depends on the step-size α .

To illustrate convergence of gradient descent, we take a simple example of a smooth convex function

$$f(x) = \frac{1}{2}(x - x^*)^2.$$

By inspection the minimizer is x^* , and because this is a one-dimensional example the operator M maps a scalar x to a scalar y . The mechanics and convergence of the fixed-point iteration are illustrated in Fig. F1. From this figure, we can make a couple general observations on conditions for converge to the minimizer x^* . First, x^* must be a fixed point of M ; i.e. I and M intersect at x^* . Second, if M is either non-decreasing or non-increasing and the magnitude of its slope is less than 1, the fixed-point iteration will converge to x^* . In stating the second condition, we have appealed to the fact that our example M maps a scalar to a scalar, so we can talk

about M being increasing or decreasing with x and the slope of M has meaning. For generalization to n -dimensional mappings see Appendix F.3.

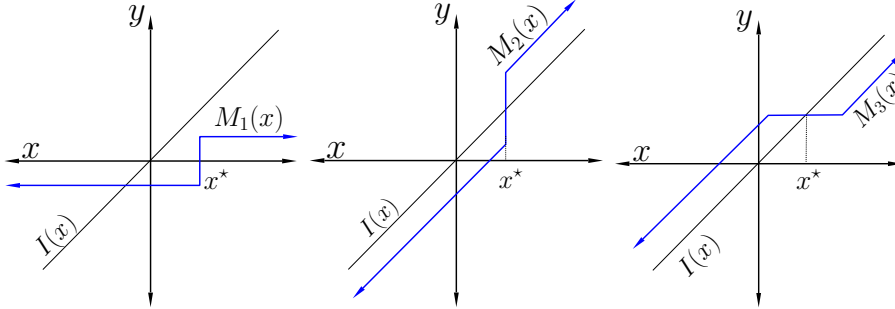


Figure F2. The three graphs illustrate construction of the proximal operator of $f(x) = |x - a|$. Left: Illustration of $M_1(x) = \partial f(x)$. Middle: Illustration of $M_2(x) = (I + \alpha \partial f)(x)$. Finally, inversion of M_2 is simply a matter of reflecting it about the 45 degree line representing $I(x)$. Right: Illustration of $M_3(x) = (I + \alpha \partial f)^{-1}(x) \equiv \text{prox}_{\alpha f}(x)$.

Appendix F.2. The proximal point algorithm for non-smooth optimization

The proximal mapping discussed in Sec. 2.3 arises from the backward Euler step for gradient descent

$$x^{(k+1)} = x^{(k)} - \alpha \partial f(x^{(k+1)}), \quad (\text{F.2})$$

which differs from Eq. (F.1) in that the gradient is replaced by the sub-differential and the sub-differential is evaluated at $x^{(k+1)}$ instead of $x^{(k)}$. Solving for $x^{(k+1)}$, can be performed with operator algebra

$$\begin{aligned} x^{(k+1)} + \alpha \partial f(x^{(k+1)}) &= x^{(k)} \\ (I + \alpha \partial f)x^{(k+1)} &= x^{(k)} \\ x^{(k+1)} &= (I + \alpha \partial f)^{-1}x^{(k)} = \text{prox}_{\alpha f}(x^{(k)}), \end{aligned}$$

where

$$\text{prox}_{\alpha f}(x) \equiv \underset{x'}{\operatorname{argmin}} \left\{ \alpha f(x') + \frac{1}{2} \|x - x'\|_2^2 \right\}. \quad (\text{F.3})$$

From the above derivation, the fixed-point operator for the proximal point algorithm is

$$M(x) = (I + \alpha \partial f)^{-1}x,$$

which can be understood in an intuitive way by breaking down its computation with a simple graphical example.

The series of graphs in Fig. F2 shows the steps to deriving the proximal operator for a simple one-dimensional non-smooth convex function

$$f(x) = |x - x^*|,$$

which, again, has a minimum value of zero at x^* . Going from left to right, the first graph shows ∂f which has a vertical segment at x^* corresponding to the multi-valuedness of the sub-differential. The second graph illustrates $I + \alpha \partial f$. For the third

and final graph, operator inversion is performed, which simply involves exchanging x and y or reflection about the 45 degree line. Note that the vertical line segment becomes horizontal and the proximal operator is single-valued.

The graphical derivation in Fig. F2 also makes clear a couple of properties of the proximal mapping of convex functions, which are possibly non-smooth, and that have a finite minimum. First, the proximal mapping converges for any α . The argument that this is the case goes as follows: the subdifferential of any convex function f is non-decreasing as x increases; thus $I + \alpha\partial f$ is strictly increasing with slope greater than or equal to 1; and this in turn implies that $(I + \alpha\partial f)^{-1}$ is non-decreasing with slope between zero and one, avoiding the red zones indicated in Fig. F1. Second, the proximal mapping is single-valued: $I + \alpha\partial f$ cannot have any horizontal segments because adding the identity to a non-decreasing function yields a strictly increasing function, thus reflection about the 45 degree line does not allow $(I + \alpha\partial f)^{-1}$ to have any vertical segments, which would indicate multi-valuedness.

Appendix F.3. Monotone operators, the Lipschitz constant, and the resolvent

[When this comes up in the saddle point discussion point out that the monotone operator is not a necessarily a gradient]

For general operators M that map n -dimensional vectors to n -dimensional vectors, the concept of non-decreasing or non-increasing in one-dimension is replaced by monotonicity. A monotone operator satisfies the condition

$$(M(u) - M(v))^{\top}(u - v) \geq 0 \text{ for all } u, v. \quad (\text{F.4})$$

The gradient of a convex function is an example of a monotone operator. The reason why we need the concept of a monotone operator is that it is more general; not all monotone operators can be written as a gradient of a convex function. The one-dimensional concept of slope is replaced by the Lipschitz constant, which is the smallest positive real number L such that

$$\|M(u) - M(v)\|_2 \leq L\|u - v\|_2 \text{ for all } u, v. \quad (\text{F.5})$$

Note that we break the convention that capital letters are operators or matrices in the case of L . If $L < 1$, M is a contraction, and if $L \leq 1$, M is non-expansive. If M is a contraction, it has a fixed point and fixed point iteration will arrive at it. The latter is seen easily by letting v be the fixed point: repeatedly applying M to v will yield v , and as a result $M(u)$ is at least a factor $L < 1$ closer to v than is u . If M is merely non-expansive, it may or may not have a fixed point and fixed point iteration might work. Monotone operators can be combined to form other monotone operators thereby generating new fixed point algorithms. Gradient descent and the proximal point algorithms, which combine the monotone operators I and ∂f , are examples of this.

As described in Refs. [6, 24] the CPPD algorithm can also be written as fixed point iteration. This requires two generalizations from the proximal point algorithm. The first generalization is the monotone operator called the resolvent R , formed from the operator F by

$$R = (I + \alpha F)^{-1}.$$

If F is monotone, R is non-expansive. The proximal operator is the resolvent of ∂f , but R is more general than prox because F may not be the subdifferential of a convex

function. Even so, iteration with R is still called the proximal point algorithm. The second generalization is the use of a generalized distance metric defined by the positive symmetric matrix B which generalizes Eq. (F.5)

$$\|M(u) - M(v)\|_B \leq L\|u - v\|_B, \quad \|u\|_B \equiv \sqrt{u^\top B u}. \quad (\text{F.6})$$

The generalized proximal point algorithm is

$$u^{(k+1)} = (B + \alpha F)^{-1} B u^{(k)},$$

which reduces to the proximal point algorithm if $B = I$.

The CPPD algorithm for solving

$$\min_x, \max_\lambda \{ \lambda^\top A x - f^*(\lambda) \}$$

is an instance of the generalized proximal point algorithm, where

$$B = \begin{pmatrix} T^{-1} & -A^\top \\ -A & \Sigma^{-1} \end{pmatrix}, \quad \alpha = 1, \quad F = \begin{pmatrix} 0 & A^\top \\ -A & \partial f^* \end{pmatrix}, \quad u = \begin{pmatrix} x \\ \lambda \end{pmatrix}.$$

Substituting these expressions into Eq. (F.6) yields the CPPD algorithm as written in Eq. (26).

Appendix G. CPPD step parameter computation

When it comes to realizing various instances of the CPPD algorithm, one of the more complicated aspects of the implementation is computing the step matrix mappings Σ and T from the system matrix A . This topic is quite broad and problem dependent. We do not attempt to cover all possibilities. We summarize only our experience in applying CPPD to optimization problems of interest for X-ray tomographic applications.

Recall from Sec. 2.2.4 and Appendix F that Σ and T are positive symmetric matrices and they must satisfy the condition that B is also positive and symmetric, where

$$B = \begin{pmatrix} T^{-1} & -A^\top \\ -A & \Sigma^{-1} \end{pmatrix}. \quad (\text{G.1})$$

We discuss three cases: scalar steps; a diagonal step matrix mapping; and a non-diagonal step matrix mapping that preconditions the CPPD iteration.

Scalar step sizes The original CPPD paper [1] employed scalar steps

$$\Sigma = \sigma I, \quad T = \tau I,$$

where σ and τ are positive real numbers, satisfying the condition

$$\sigma\tau < 1/L^2, \quad L \equiv \|A\|_2.$$

Note that this condition is equivalent to the condition that M is a positive matrix. The computation of L can be time consuming, but it can be performed ahead of the CPPD iteration and stored for the given system matrix A . The CPPD algorithms presented in [1] included σ and τ fixed as a function of iteration number and Nesterov

accelerated versions, where σ and τ vary with iteration number in such a way that can improved convergence rates. Another reference that we found interesting was an adaptive scheme for balancing primal and dual progress proposed by Goldstein *et al.* [25].

We have had some experience in implementing the CPPD Nesterov acceleration schemes [26]; however, when we performed empirical testing of various implementations of CPPD for gradient sparsity regularization [13], we found that fixing σ and τ as a function of iteration number performed just as efficiently if not more so than implementations involving various forms of acceleration. We have since rarely employed CPPD with Nesterov acceleration or other schemes [25] for adapting σ and τ as a function of iteration number. One important piece of information that resulted from testing the adaptive scheme of Goldstein *et al.* [25] is that the ratio of the step sizes σ and τ is an important tuning parameter as demonstrated in the results shown in Sec. 3. When using scalar steps, we set σ and τ according to

$$\sigma = \rho/L, \quad \tau = 1/(\rho L),$$

and the step size ratio ρ is varied to find the setting that leads to the most rapid convergence. Note that these settings violate the strict inequality condition, but in practice we have never encountered a situation where this setting has led to non-convergence CPPD iteration.

As a practical tip, it is helpful to test the computation of the scalars σ and τ , because they can involve a complicated power method implementation especially when the optimization problem of interest involves a system matrix A that is formed by stacking many matrices. The step scalars σ and τ are set to values that multiply to $1/L^2$. Any error that leads to L significantly less than $\|A\|_2$ will be discovered immediately, because it will lead to the product $\sigma\tau$ being too large and divergent iteration. On the other hand, L larger than $\|A\|_2$ will not be easy to discover because the CPPD algorithm will still converge to the solution of the optimization problem of interest. It will, however, do so more slowly than the case where L is computed correctly. An easy test is to attempt the CPPD iteration with $L = a\|A\|_2$ where $0 < a < 1$. If convergent behavior is observed for $a < 0.8$, then this is an indication that there is a likely an error in the computation of L . It is not a definitive test because the convergence condition inequality is not tight. So it is actually possible, in our experience, to have convergent CPPD iteration for $0.8 < a < 1.0$. A side benefit to performing this test is that a "safe" value $a < 1.0$ can be empirically discovered that leads to slightly faster CPPD convergence than the $a = 1.0$ case.

Diagonal step matrices Pock and Chambolle proposed diagonal step matrices in [7]

$$\begin{aligned} \Sigma &= \text{diag} ((|A|1)^{-1}) \\ T &= \text{diag} ((|A|^\top 1)^{-1}), \end{aligned}$$

where the $\text{diag}(\cdot)$ operator yields a diagonal matrix with the diagonal elements assigned to the components of the vector in the argument. The absolute value $|\cdot|$ and inverse $(\cdot)^{-1}$ operators are applied element-wise to the matrix and vector arguments. As A is an m by n matrix, the symbol 1 is interpreted as a n -vector and m -vector with all components set to 1 the Σ and T equation, respectively. The diagonal step matrices have two advantages: they are more efficiently computed than the scalar step

sizes because they involve single matrix-vector products between $|A|$ and 1 instead of repeated matrix-vector products required in the iterative power method; and they perform preconditioning that may be significant for specific problems. The efficiency of the diagonal step matrix computation enables application of the CPPD algorithm to problems where the optimization problem of interest is changing as a function of iteration number because it is feasible to re-compute the step matrices at every iteration or every few iterations. We have taken advantage of this efficiency property in our mirrored convex/concave (MOCCA) algorithm which address optimization problems that can be written as a combination of non-convex smooth and convex non-smooth functions [27].

In implementing the diagonal step matrices, we have encountered a situation where they can be more difficult to compute than the scalar step sizes. If the system matrix A is a product of matrices that may have negative matrix elements, it can be difficult to obtain $|A|$. Note that this situation is not a problem for the scalar step sizes because only the matrix A is needed in the power method. If A is a product of matrices

$$A = \Pi_i A_i,$$

it can be shown by repeated use of the Cauchy-Schwarz inequality that

$$|A| \leq \Pi_i |A_i|.$$

Taking the product of the absolute value of the matrix factors provides an upperbound on $|A|$, and using this upperbound for the diagonal step matrices will yield conservative steps that result in convergent iteration. Use of this upperbound is practical when computing $|A_i|$ is efficient and when it does not result in too much loss of efficiency in the CPPD convergence. We have found this upperbound to be useful in applying MOCCA to spectral CT image reconstruction [28], where the system matrix involves a product of matrices including a preconditioning matrix that has both negative and positive matrix elements.

The diagonal step matrices have proven useful, but we do not show examples of their use in this article. When implementing diagonal step matrices it is important to make use of the the step size ratio parameter ρ , discussed for scalar steps, in order to maximize algorithm efficiency.

Non-diagonal step matrices for preconditioning As discussed in Sec. 2.2.5, a non-diagonal preconditioning step matrix T can be derived by approximating the inverse of $(A^\top A)$

$$\Sigma = \sigma I, \quad T \approx (A^\top A)^{-1},$$

where the scalar σ is determined after T is specified

$$\sigma = 1/\|TA^\top A\|_2. \quad (\text{G.2})$$

A classic method of obtaining an approximate matrix inverse is to use a truncated eigenvector expansion. The matrix $(A^\top A)$ is symmetric and positive semi-definite, and its eigenvector decomposition is

$$A^\top A = U E U^\top,$$

Algorithm 3 Modified power method for finding K eigenvectors of $A^\top A$. The parameter N_{power} is the number of iterations taken for the power method. The input to the algorithm is the matrix A and the output are the eigenvectors u_k and corresponding eigenvalues e_k .

```

1: k=0
2: while  $k < K$  do
3:   Initialize  $u_k$ 
4:   j=0
5:   while  $j < N_{\text{power}}$  do
6:      $u_k \leftarrow A^\top A u_k$ 
7:     i=0
8:     while  $i < k - 1$  do
9:        $u_k \leftarrow u_k - (u_k^\top u_i) u_i$ 
10:       $i \leftarrow i + 1$ 
11:    end while
12:     $e_k \leftarrow \|u_k\|_2$ 
13:     $u_k \leftarrow u_k / e_k$ 
14:     $j \leftarrow j + 1$ 
15:  end while
16:   $k \leftarrow k + 1$ 
17: end while

```

where U is an orthogonal matrix and E is diagonal with non-negative eigenvalues, e_i , on the diagonal; without loss of generality, the eigenvalues are sorted from largest to smallest. Using a truncated series, the matrix T is expressed

$$T = \frac{I}{e_K} + \sum_{i=1}^{K-1} u_i \left(\frac{1}{e_i} - \frac{1}{e_K} \right) u_i^\top \approx (A^\top A)^{-1}, \quad (\text{G.3})$$

where I is the identity matrix; K is the number of eigenvectors used in the expansion, and the eigenvectors can be found by simple modification of the power method, described in Algorithm 3.

For the LSQ problem, presented in Sec. Appendix I.1, the matrix A is assigned to X , the discrete-to-discrete approximation of the X-ray transform. Implementation of non-diagonal preconditioning with X requires some specific understanding of the structure of X . The eigenvalues of $X^\top X$ vary over orders of magnitude, see for example Ref. [18], leading to slow convergence of first-order iterative algorithms. The eigenvalues of the first few eigenvectors decreases strongly, so building an approximate inverse of $X^\top X$ using even the first few eigenvectors can increase the efficiency of the CPPD iteration substantially. Also, the leading eigenvectors tend to dominate the CPPD image iterates at low iteration number. Careful design of T can improve the image quality of the images at low iteration number in addition to improving convergence speed.

The non-negative and relatively smooth nature of the sensing matrix X is such that, in general, the largest eigenvalue corresponds to an eigenvector with no spatial nodes. As the eigenvalues decrease, more spatial nodes are seen in the corresponding

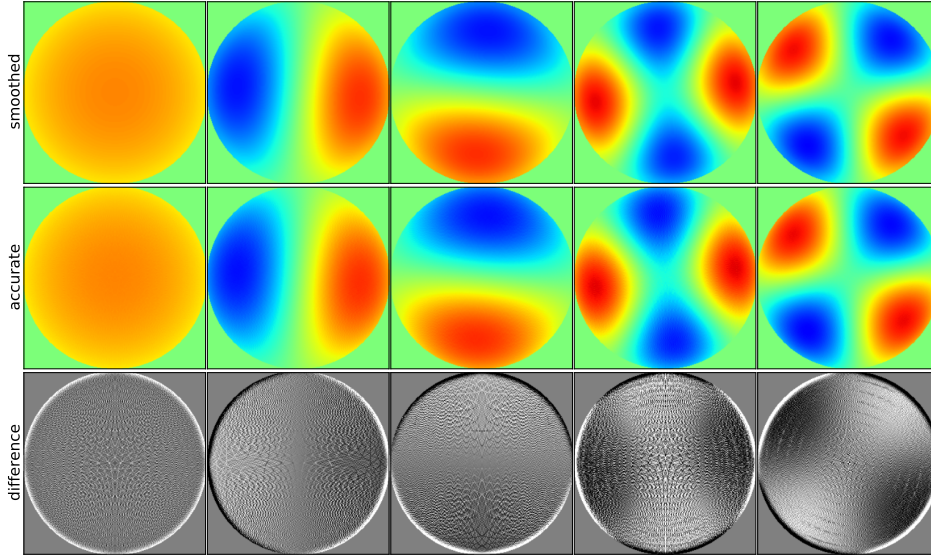


Figure G1. The first five eigenvectors of $X^\top X$ ranked by singular value, going from left to right. Top row shows the smoothed approximate eigenvectors, obtained by blurring the computed eigenvector with a gaussian of 4-pixel width. Middle row contains the corresponding numerically exact eigenvectors. Bottom row shows the difference between approximate and accurate eigenvectors; these images show the Moiré patterns that can enter the image iterates of CPPD if the accurate eigenvectors are used to form the CPPD preconditioner. The eigenvector images are shown in a color scale because it displays the eigenvector structure clearly; the color scale, blue to red, spans $[-0.01, 0.01]$. The gray scale, black to white, for the difference plots in the bottom row spans $[-0.0001, 0.0001]$.

eigenvector. Computing eigenvectors of $X^\top X$ for the configuration specified in Sec. Appendix I.1 directly illustrates this trend as seen in Fig. G1. Due to the discretization of the X-ray transform there is a small high-spatial frequency component present that can contaminate images at low iteration number with Moiré patterns. For preconditioning, we only want to account for the low-spatial frequency dependences and avoid the high-frequency Moiré patterns. Thus, in designing the T preconditioner, there is benefit to computing the approximate matrix inverse from spatially smoothed eigenvectors. To obtain such eigenvectors, the modified power method in Alg. 3 is employed with A replaced by X , and the resulting eigenvector are smoothed

$$u_k \leftarrow S u_k \quad (\text{G.4})$$

where S is a symmetric matrix that performs discrete convolution with a smooth kernel. The corresponding leading smoothed eigenvectors are shown in G1 for smoothing by a Gaussian with a width of 4 pixels. The smoothed eigenvectors capture the low-frequency behavior of the accurate eigenvectors, and they can be used in Eq. G.3 to construct the matrix T .

For the TV-LSQ problem where A consists of the stacked matrix

$$A = \begin{bmatrix} X \\ \nu \nabla \end{bmatrix},$$

the leading eigenvectors of $SX^\top XS$ are also approximate eigenvectors of $A^\top A$. The

reason for this is that these leading eigenvectors have low spatial frequency, and as a result they are all nearly in the null space of ∇ . So, once again, we can use the smoothed eigenvectors of $X^\top X$ to form non-diagonal T using Eq. (G.3). The k th eigenvalue is used to determine the parameter ν

$$\nu^2 = e_K / \|\nabla\|_2^2.$$

For TV-LSQ, smoothed eigenvectors and eigenvalues of X are computed with the modified power method. The matrix stacking combination parameter ν is then calculated. Finally, σ is obtained from Eq. (G.2).

The truncated eigenvector series in Eq. (G.3) has the advantage that it applies to non-standard CT configurations such as sparse-view or limited angular range sampling. When using standard scanning, an effective preconditioner can be derived from the fact that $X^\top X$ is equivalent to convolving with $1/r$ for X representing continuous 2D parallel-beam projection [29]. This observation leads to the cone-filter preconditioner, see for example Ramani and Fessler [30]. Even though the cone-filter is derived for 2D circular, parallel-beam CT, it should still be effective for circular, fan-beam CT with a discrete-to-discrete system matrix X . Use of the cone-filter as T is also demonstrated in Sec. Appendix I.1. Finally, we point out that the step size ratio parameter, ρ , can be used with the matrix mapping steps. We did not explicitly include it in order to simplify the discussion.

Other examples of preconditioning with splitting methods applied in imaging have been discussed in the context of CT in [31]. For magnetic resonance imaging (MRI), Ref. [32] presents a preconditioner tailored to application of CPPD to MRI-based optimization problems.

Appendix H. Convergence criteria

Recall from Sec. 2.1 that the CPPD iteration solves the generic convex minimization

$$x^* = \underset{x}{\operatorname{argmin}} F(Ax).$$

Because we are interested in $F(\cdot)$ being possibly nonsmooth, useful convergence criteria based directly on the objective function $F(Ax)$ can only be done in a problem specific manner. To illustrate the issue consider F to be one of three common cases: (i) differentiable, (ii) ℓ_1 -norm, or (iii) an indicator of a convex set.

(i) If F is differentiable, the magnitude of the gradient

$$g = A^\top \nabla F(Ax)$$

provides a useful convergence criterion because $\|g\|_2$ approaches 0 as x approaches the solution. Also, if F is locally quadratic about the solution, $\|g\|_2$ is linear in the distance between x and the solution. The objective function value itself is not as useful because it requires knowledge of the minimum value of $F(Ax)$ and it is not as sensitive as the objective function gradient.

(ii) If F is the ℓ_1 -norm, one can check that zero is in the subgradient, i.e. $0 \in \partial\|Ax\|_1$, but this condition is not useful because zero is in the subgradient only when Ax is exactly zero. Otherwise, when $Ax \neq 0$ the gradient magnitude away from the solution is constant. Thus the gradient does not yield information on proximity of

x to the minimizer. The objective function itself, however, is informative in this case as long as the function minimum is known ahead of time.

(iii) If F is an indicator function, i.e. the objective function is $\delta_S(Ax)$, neither the objective function value nor its subgradient is informative. Instead one can employ a distance function that yields the distance between Ax and the closest point in the set S .

For any given F , it may be possible to employ some combination of a gradient, objective function value, and distance function to provide useful convergence criteria. What we would like to promote here instead are general convergence conditions that can be used for any problem where the CPPD iteration applies.

First-order CPPD convergence criteria

Convenient convergence conditions can be formulated from the intermediate saddle point problem Eq. (2), which we repeat here

$$\min_{x,y} \max_{\lambda} \{ \phi(y) + \lambda^\top (Ax - y) \}.$$

The solution of this optimization not only involves finding the desired x but also the dual variable λ and the splitting variable y . Repeating the conditions from Eqs. (3)-(5), the solution to the saddle problem is

$$A^\top \lambda = 0, \quad \lambda = \partial\phi(y), \quad Ax - y = 0.$$

The middle equation is already used in deriving the CPPD saddle point problem; recall that Eq. (6) only involves x and λ . So for convergence we only need to check

$$r_\tau^{(k)} \equiv A^\top \lambda^{(k)} \rightarrow 0, \tag{H.1}$$

$$r_\sigma^{(k)} \equiv Ax^{(k)} - y^{(k)} \rightarrow 0, \tag{H.2}$$

as $k \rightarrow \infty$. The equation $r_\tau = 0$ is called the transversality condition (τ for τ transversality), see for example Proposition 4.4.1 on pg. 336 of Ref. [21]. The equation $r_\sigma = 0$ is the feasibility condition, but we use a more specific name for the magnitude of the left-hand side. We call the quantity $\|r_\sigma\|_2$ the splitting gap (σ for σ plitting) because it is a measure of the difference between the splitting variable y and Ax . The first condition can be checked immediately because $\lambda^{(k)}$ is available from the CPPD iteration, but the second equation requires $y^{(k)}$ to be known. To obtain y , an extra line can be introduced into the CPPD iteration.

[Make sure to clarify the difference between $y \in \partial\phi$ and $y = \partial\phi$, especially in the Legendre Transform relations]

Recall the CPPD iteration Eq. (30)

$$\begin{aligned} x^{(k+1)} &= x^{(k)} - TA^\top \lambda^{(k)}, \\ \bar{x}^{(k+1)} &= 2x^{(k+1)} - x^{(k)}, \\ \lambda^{(k+1)} &= \text{prox}_{\sigma\phi^*}(\lambda^{(k)} + \sigma A\bar{x}^{(k+1)}). \end{aligned} \tag{H.3}$$

The last line is equivalent to

$$(I + \sigma\partial\phi^*)\lambda^{(k+1)} = \lambda^{(k)} + \sigma A\bar{x}^{(k+1)}, \tag{H.4}$$

and there are two ways to proceed depending on whether it is easier to compute (i) prox_{ϕ^*} or (ii) prox_{ϕ} .

(i) prox_{ϕ^*} is simpler: Using the fact that $y = \partial\phi^*(\lambda)$, Eq. (H.4) becomes

$$\lambda^{(k+1)} + \sigma y^{(k+1)} = \lambda^{(k)} + \sigma A\bar{x}^{(k+1)}. \quad (\text{H.5})$$

Solving for $y^{(k+1)}$ yields

$$y^{(k+1)} = \frac{1}{\sigma}(\lambda^{(k)} - \lambda^{(k+1)}) + A\bar{x}^{(k+1)}.$$

This update for y can be appended to the CPPD iteration after Eq. (H.3). As a side note, using the y -update to directly write an update for the splitting gap yields,

$$\begin{aligned} r_{\sigma}^{(k+1)} &= y^{(k+1)} - Ax^{(k+1)} \\ &= \frac{1}{\sigma}(\lambda^{(k)} - \lambda^{(k+1)}) + A(2x^{(k+1)} - x^{(k)}) - Ax^{(k+1)} \\ &= \frac{1}{\sigma}(\lambda^{(k)} - \lambda^{(k+1)}) + Ax^{(k+1)} - Ax^{(k)}. \end{aligned}$$

This expression for the splitting gap is identical to what is called the ‘‘dual residual’’ in Ref. [25].

(ii) prox_{ϕ} is simpler: In this case, the Moreau identity can be exploited to obtain $\text{prox}_{\sigma\phi^*}$

$$\text{prox}_{\sigma\phi^*}(\lambda) + \sigma \text{prox}_{\phi/\sigma}(\lambda/\sigma) = \lambda. \quad (\text{H.6})$$

Alternatively, and equivalently, a modified version of the CPPD iteration can be directly derived. Using the fact that $y = \partial\phi^*(\lambda)$ and $\lambda = \partial\phi(y)$, Eq. (H.4) becomes

$$(\partial\phi + \sigma)y^{(k+1)} = \lambda^{(k)} + \sigma A\bar{x}^{(k+1)},$$

or

$$y^{(k+1)} = \text{prox}_{\phi/\sigma}(\lambda^{(k)}/\sigma + A\bar{x}^{(k+1)}). \quad (\text{H.7})$$

This line can be inserted before Eq. (H.3) in the CPPD iteration, then the variable y is available to compute the convergence condition Eq. (H.2). But if this line is used to obtain y , it is not necessary to perform the additional prox operation in Eq. (H.3). The λ -update can be obtained by solving for $\lambda^{(k+1)}$ in Eq. (H.5). This version of the CPPD algorithm becomes

$$x^{(k+1)} = x^{(k)} - TA^{\top}\lambda^{(k)}, \quad (\text{H.8})$$

$$\bar{x}^{(k+1)} = 2x^{(k+1)} - x^{(k)},$$

$$y^{(k+1)} = \text{prox}_{\phi/\sigma}(\lambda^{(k)}/\sigma + A\bar{x}^{(k+1)}),$$

$$\lambda^{(k+1)} = \lambda^{(k)} + \sigma(A\bar{x}^{(k+1)} - y^{(k+1)}). \quad (\text{H.9})$$

The CPPD algorithm as written in Eqs. (H.8)-(H.9) connects well with the convergence criteria, and, thus, reveals the trade-off between the step parameters σ and T . The x -update in Eq. (H.8) adjusts x in such a way that reduces $|A^{\top}\lambda|$, and similarly, the λ -update in Eq. (H.9) adjusts λ so that $|Ax - y|$ is reduced. Choosing T large increases progress toward $r_{\tau}^{(k)} \rightarrow 0$, i.e. Eq. (H.1), and conversely choosing σ large increases progress toward $r_{\sigma}^{(k)} \rightarrow 0$, i.e. Eq. (H.2).

The primal-dual gap

In our first article that demonstrated the use of CPPD for optimization problem prototyping for CT image reconstruction [3], we proposed the conditional primal-dual (cPD) gap as a convergence check. In that paper, we considered the convex optimization framework put forth in Ref. [1], where the general minimization problem was written

$$x^* = \operatorname{argmin}_x \{\phi(Ax) + \eta(x)\},$$

and both ϕ and η are convex functions.

In the simplified framework discussed here this gap is derived from the primal problem, involving minimization over x ,

$$x^* = \operatorname{argmin}_x \phi(Ax),$$

and the dual problem, involving maximization over λ ,

$$\lambda^* = \operatorname{argmax}_\lambda \{-\delta(A^\top \lambda = 0) - \phi^*(\lambda)\},$$

where the dual problem is obtained by performing the minimization over x in Eq. (6). For a given x and λ the primal-dual gap is the difference between these two objective functions

$$\text{PD}(x, \lambda) = \phi(Ax) + \delta(A^\top \lambda = 0) + \phi^*(\lambda).$$

This function is positive, when x and λ are not solutions of their respective minimization and maximization problems. When a solution to both is obtained,

$$\text{PD}(x^*, \lambda^*) = 0.$$

This condition, however, is not of much practical use for a convergence criterion because it involves at least one indicator function, which can have infinite value for finite x or λ .

A practical condition can be obtained by splitting both objective functions into bounded and indicator functions

$$\phi(Ax) = \phi_{\text{bp}}(Ax) + \sum_i \delta(Ax \in \mathcal{P}_i), \quad \phi^*(\lambda) = \phi_{\text{bd}}^*(\lambda) + \sum_j \delta(\lambda \in \mathcal{D}_j).$$

[Make sure to explain all variations in indicator notation] Progress toward satisfying each of the indicators can be measured by computing distance to each of the primal convex constraint sets \mathcal{P}_i , dual constraint sets \mathcal{D}_j , and $A^\top \lambda$ from 0. The remaining portion of the primal dual gap, which we called the conditional primal-dual gap, is

$$\text{cPD}(x, \lambda) = \phi_{\text{bp}}(Ax) + \phi_{\text{bd}}^*(\lambda).$$

This quantity is bounded for finite x and λ , and it approaches zero as $x \rightarrow x^*$ and $\lambda \rightarrow \lambda^*$. Because the indicators are taken away in forming cPD, this function can have, in general, both positive and negative values. So for checking convergence the absolute value of this function should be checked.

Use of $|\text{cPD}(x, \lambda)|$ as a convergence criterion has trade-offs compared with use of r_σ and r_τ . The conditional primal-dual gap does not require computation of the splitting variable y , but it can yield difficult to interpret curves because cPD can oscillate about zero and its absolute value is used to check convergence. In this article, we employ r_σ and r_τ exclusively.

Appendix I. Derivation of CPPD instances

In this appendix, the derivation for the specific instances of the CPPD algorithm are derived. The generic convex optimization problem is

$$x^* = \underset{x}{\operatorname{argmin}} \phi(Ax). \quad (\text{I.1})$$

The CPPD iteration for solving this equation is

$$\begin{aligned} x^{(k+1)} &= x^{(k)} - TA^\top \lambda^{(k)}, \\ \bar{x}^{(k+1)} &= 2x^{(k+1)} - x^{(k)}, \\ \lambda^{(k+1)} &= \operatorname{prox}_{\sigma\phi^*}(\lambda^{(k)} + \sigma A\bar{x}^{(k+1)}), \\ y^{(k+1)} &= \frac{1}{\sigma}(\lambda^{(k)} - \lambda^{(k+1)}) + A\bar{x}^{(k+1)}. \end{aligned}$$

As explained in Appendix H, the last line that updates the splitting variable y is included for computing the splitting gap, which is a convergence metric. It is not strictly needed for obtaining the solution estimate. In the case that it is easier to compute prox_ϕ than $\operatorname{prox}_{\phi^*}$, see Eq. (H.6).

Appendix I.1. Least-squares (LSQ) minimization

The first optimization problem is LSQ minimization

$$f^* = \underset{f}{\operatorname{argmin}} \frac{1}{2} \|Xf - g\|_2^2, \quad (\text{I.2})$$

where X is the discrete X-ray transform; f represents the image expansion coefficients; and g is the projection data vector. Derivation of CPPD for this problem is straightforward because the potential function ϕ is differentiable. Making the following associations,

$$A = X, \quad x = f, \quad \phi(y) = \frac{1}{2} \|y - g\|_2^2,$$

puts Eq. (I.2) in the form of Eq. (I.1). To obtain the CPPD updates, the Legendre transform of ϕ and the *prox* mappings are needed

$$\phi^*(y) = \frac{1}{2} \|y\|_2^2 + y^\top g, \quad \operatorname{prox}_{\sigma\phi^*}(\lambda) = \frac{\lambda - \sigma g}{1 + \sigma}. \quad (\text{I.3})$$

Substituting into the CPPD iteration equations, yields the CPPD-LSQ updates

$$\begin{aligned} f^{(k+1)} &= f^{(k)} - TX^\top \lambda^{(k)}, \\ \bar{f}^{(k+1)} &= 2f^{(k+1)} - f^{(k)}, \\ \lambda^{(k+1)} &= \left(\lambda^{(k)} + \sigma(X\bar{f}^{(k+1)} - g) \right) / (1 + \sigma), \\ y^{(k+1)} &= \frac{1}{\sigma}(\lambda^{(k)} - \lambda^{(k+1)}) + A\bar{f}^{(k+1)}. \end{aligned}$$

Appendix I.2. Total variation penalized least-squares (TVLSQ)

For the next algorithm instance, we derive the CPPD update formulas for TVLSQ.

$$f^* = \operatorname{argmin}_f \left\{ \frac{1}{2} \|Xf - g\|_2^2 + \beta \|Df\|_1 \right\}, \quad (\text{I.4})$$

where β is the scalar penalty parameter and D is a finite-differencing approximation of the image gradient. Addressing this optimization problem, while interesting in its own right, serves as a stepping stone to the algorithm instance for the next problem, which is TV-constrained LSQ (TVCLSQ). The associations for the TVLSQ optimization problem are

$$A = \begin{pmatrix} X \\ \nu D \end{pmatrix}, \quad x = f, \quad \phi(y) = \frac{1}{2} \|y_s - g\|_2^2 + (\beta/\nu) \|y_g\|_1,$$

where

$$\nu = \|X\|_2 / \|D\|_2;$$

y_s and y_g are the splitting variables for the X-ray transform and image gradient, respectively, and

$$y = \begin{pmatrix} y_s \\ y_g \end{pmatrix},$$

where s and g stand for “sinogram” and “gradient”, respectively. We denote the two terms of the potential ϕ_s and ϕ_g , where

$$\phi_s(y_s) = \frac{1}{2} \|y_s - g\|_2^2, \quad \phi_g(y_g) = (\beta/\nu) \|y_g\|_1.$$

Note that in fitting this optimization problem in the $\phi(Ax)$ form, it is necessary to “stack” the linear transforms, X and νD , to form the matrix A : The matrix X is m by n and in two dimensions D is $2n$ by n ; the number of columns of both matrices is the same number n , the number of image pixels. The first m rows of A are the same as the m rows of X , and rows $m+1$ through $m+2n$ of A are the rows of νD . The constant ν is introduced as a factor multiplying D and dividing β so that the matrices X and νD will have the same magnitude, i.e. largest singular value. This normalization factor is useful because the step size parameters σ and T depend on A , and changing the units of X or D will accordingly alter the CPPD iteration performance without this normalization.

Because the potential function ϕ separates into ϕ_s and ϕ_g , the proximal mapping separates also. This can be shown by explicitly writing the optimization problem corresponding to $\operatorname{prox}_{\sigma\phi^*}$

$$\begin{aligned} \operatorname{prox}_{\sigma\phi^*}(\lambda) &= \operatorname{argmin}_{\lambda'} \left\{ \sigma\phi^*(\lambda') + \frac{1}{2} \|\lambda' - \lambda\|_2^2 \right\} \\ &= \operatorname{argmin}_{\lambda'_s, \lambda'_g} \left\{ \sigma\phi_s^*(\lambda'_s) + \frac{1}{2} \|\lambda'_s - \lambda_s\|_2^2 + \sigma\phi_g^*(\lambda'_g) + \frac{1}{2} \|\lambda'_g - \lambda_g\|_2^2 \right\} \\ &= \begin{pmatrix} \operatorname{prox}_{\sigma\phi_s^*}(\lambda_s) \\ \operatorname{prox}_{\sigma\phi_g^*}(\lambda_g) \end{pmatrix}. \end{aligned}$$

Accordingly, the CPPD iteration for TVLSQ takes the form

$$\begin{aligned}
f^{(k+1)} &= f^{(k)} - T(X^\top \lambda_s^{(k)} + \nu D^\top \lambda_g^{(k)}), \\
\bar{f}^{(k+1)} &= 2f^{(k+1)} - f^{(k)}, \\
\lambda_s^{(k+1)} &= \text{prox}_{\sigma\phi_s^*}(\lambda_s^{(k)} + \sigma X \bar{f}^{(k+1)}), \\
\lambda_g^{(k+1)} &= \text{prox}_{\sigma\phi_g^*}(\lambda_g^{(k)} + \sigma \nu D \bar{f}^{(k+1)}), \\
y_s^{(k+1)} &= \frac{1}{\sigma}(\lambda_s^{(k)} - \lambda_s^{(k+1)}) + X \bar{f}^{(k+1)}, \\
y_g^{(k+1)} &= \frac{1}{\sigma}(\lambda_g^{(k)} - \lambda_g^{(k+1)}) + \nu D \bar{f}^{(k+1)}.
\end{aligned}$$

where $\text{prox}_{\sigma\phi_s^*}$ and $\text{prox}_{\sigma\phi_g^*}$ need to be evaluated. The first proximal mapping is the same as Eq. (I.3).

For the second proximal mapping, it is first necessary to obtain ϕ_g^* . Recall, $\phi_g = (\beta/\nu)\|y_g\|_1$, and from Appendix C the convex conjugate is

$$\phi_g^*(\lambda) = \delta(\|\lambda\|_\infty \leq \beta/\nu).$$

As ϕ_g^* is an indicator function, $\text{prox}_{\sigma\phi_g^*}$ is projection of the input variable λ onto the convex set described by $\|\lambda\|_\infty \leq \beta/\nu$, which is implemented component-wise with the formula for the i th component given by

$$\left[\text{prox}_{\sigma\phi_g^*}(\lambda_i)\right]_i = \begin{cases} -\beta/\nu & \lambda_i \leq -\beta/\nu \\ \lambda_i & -\beta/\nu < \lambda_i < \beta/\nu \\ \beta/\nu & \beta/\nu \leq \lambda_i \end{cases}.$$

Equivalently, this proximal mapping can be written as

$$\text{prox}_{\sigma\phi_g^*}(\lambda) = \frac{(\beta/\nu)\lambda}{\max(\beta/\nu, |\lambda|)}, \quad (\text{I.5})$$

where the max function operates component-wise on $|\lambda|$. This latter form is slightly more convenient than the previous form, and it avoids divide-by-zero since the minimum component value of the denominator is β/ν .

Installing the specific proximal mappings, the CPPD update equations for TVLSQ become

$$\begin{aligned}
f^{(k+1)} &= f^{(k)} - T(X^\top \lambda_s^{(k)} + \nu D^\top \lambda_g^{(k)}), \\
\bar{f}^{(k+1)} &= 2f^{(k+1)} - f^{(k)}, \\
\lambda_s^{(k+1)} &= \frac{\lambda_s^{(k)} + \sigma(X \bar{f}^{(k+1)} - g)}{1 + \sigma}, \\
\lambda_g^+ &= \lambda_g^{(k)} + \sigma \nu D \bar{f}^{(k+1)}, \\
\lambda_g^{(k+1)} &= \frac{(\beta/\nu)\lambda_g^+}{\max(\beta/\nu, |\lambda_g^+|)}, \\
y_s^{(k+1)} &= \frac{1}{\sigma}(\lambda_s^{(k)} - \lambda_s^{(k+1)}) + X \bar{f}^{(k+1)}, \\
y_g^{(k+1)} &= \frac{1}{\sigma}(\lambda_g^{(k)} - \lambda_g^{(k+1)}) + \nu D \bar{f}^{(k+1)}.
\end{aligned}$$

The discussion on setting the step parameters in Appendix G apply to determining the specific form of T and σ in these update equations. In particular, we emphasize a few implementation issues. As discussed in Appendix G, whichever form of T and σ is selected, it is important to empirically tune the step-size ratio parameter ρ because convergence rates can vary by orders of magnitude as a function of ρ . Also, in this presentation of the CPPD updates for TVLSQ we have selected one particular method for stacking and normalization of the linear transforms X and D . While other forms of transform normalization could be used, it is important to do this in one form or another. If this is not done, algorithm performance will vary with the physical units selected for formulating X and D . For optimization problems involving more than two linear transforms, the stacking and normalization generalizes in a straight-forward manner.

Appendix I.3. Total variation constrained least-squares (TVCLSQ)

A related optimization problem to TVLSQ is total variation constrained least-squares (TVCLSQ), which is formulated as

$$f^* = \operatorname{argmin}_f \left\{ \frac{1}{2} \|Xf - g\|_2^2 + \delta(\|Df\|_1 \leq \gamma) \right\},$$

where the indicator function encodes a constraint that the image TV is bounded above by γ . The TVCLSQ optimization problem is closely related to that of TVLSQ. In fact, if the constraint parameter γ of TVCLSQ and penalty parameter β of TVLSQ are chosen appropriately, the solutions will be identical. The associations for putting the TVCLSQ optimization problem in the generic form of Eq. (I.1) are

$$A = \begin{pmatrix} X \\ \nu D \end{pmatrix}, \quad x = f, \quad \phi(y) = \frac{1}{2} \|y_s - g\|_2^2 + \delta(\|y_g\|_1 \leq \nu\gamma),$$

where ν is the normalization factor for D as defined in the presentation of the TVLSQ problem; and y_s and y_g are the splitting variables for the X-ray transform and image gradient, respectively. The TVCLSQ objective is split in two terms

$$\begin{aligned} \phi_s(y_s) &= \frac{1}{2} \|y_s - g\|_2^2, \\ \phi_{gc}(y_g) &= \delta(\|y_g\|_1 \leq \nu\gamma) \end{aligned}$$

Because ϕ_s is the same as it is in the TVLSQ example, we need only discuss ϕ_{gc} (“gc” stands for “gradient constraint”), which has been altered to reflect the constraint form.

The new proximal mapping needed for TVCLSQ is $\operatorname{prox}_{\sigma F_{gc}^*}$, which is related to $\operatorname{prox}_{\phi_{gc}}$ through the Moreau identity

$$\begin{aligned} \operatorname{prox}_{\sigma\phi_{gc}^*}(\lambda_g) &= \lambda_g - \sigma \operatorname{prox}_{F_{gc}/\sigma}(\lambda_g/\sigma), \\ &= \lambda_g - \sigma \operatorname{proj}(\lambda_g/\sigma, \|\lambda_g/\sigma\|_1 \leq \nu\gamma), \\ &= \lambda_g - \operatorname{proj}(\lambda_g, \|\lambda_g\|_1 \leq \nu\gamma\sigma). \end{aligned} \tag{I.6}$$

We write the optimization problem corresponding to the projection (or proximal mapping) on the right-hand side of Eq. (I.6)

$$\operatorname{proj}(\lambda_g, \|\lambda_g\|_1 \leq \nu\gamma\sigma) = \operatorname{argmin}_\lambda \left\{ \frac{1}{2} \|\lambda - \lambda_g\|_2^2 + \delta(\|\lambda\|_1 \leq \nu\gamma\sigma) \right\}. \tag{I.7}$$

In evaluating this optimization problem, there are two cases:

$\|\lambda_g\|_1 \leq \nu\gamma\sigma$: When this inequality is satisfied,

$$\text{proj}(\lambda_g, \|\lambda_g\|_1 \leq \nu\gamma\sigma) = \lambda_g.$$

The right-hand side of Eq. (I.6) is then $\lambda_g - \lambda_g$, and accordingly,

$$\text{if } \|\lambda_g\|_1 < \nu\gamma\sigma, \quad \text{prox}_{\sigma\phi_{gc}^*}(\lambda_g) = 0. \quad (\text{I.8})$$

$\|\lambda_g\|_1 > \nu\gamma\sigma$: In this case, y_g needs to be projected onto the ℓ_1 -ball of size $\nu\gamma\sigma$. An efficient sorting-based algorithm that can perform $\text{proj}(\lambda_g, \|\lambda_g\|_1 \leq \nu\gamma\sigma)$ is available in Ref. [33]. We also present an alternative that takes advantage of one of the powerful aspects of splitting, i.e. separation the potential ϕ from large linear transforms. In this non-trivial case where $\|\lambda_g\|_1 > \nu\gamma\sigma$ the constrained optimization problem of Eq. (I.7) is equivalent to the following unconstrained optimization problem

$$\lambda'_g = \underset{\lambda}{\text{argmin}} \left\{ \frac{1}{2} \|\lambda - \lambda_g\|_2^2 + \beta \|\lambda\|_1 \right\}, \quad (\text{I.9})$$

for an appropriate choice of penalty parameter β . where we use a different solution notation, λ'_g , because we do not know *a priori* which value of β yields $\lambda'_g = \text{proj}(\lambda_g, \|\lambda_g\|_1 \leq \nu\gamma\sigma)$. This optimization problem is the proximal mapping for the ℓ_1 -norm. Equation (I.9) evaluates to a shrinkage operation

$$\lambda'_g = \text{prox}_{\beta\|\cdot\|_1}(\lambda_g) = \text{shrink}(\lambda_g, \beta),$$

where β is selected to be the value that shrinks λ_g until it satisfies $\|\lambda_g\|_1 = \nu\gamma\sigma$. Thus the equation for β becomes

$$\|\text{shrink}(\lambda_g, \beta)\|_1 - \nu\gamma\sigma = 0. \quad (\text{I.10})$$

This problem can be readily solved numerically by any 1D root-finding algorithm, e.g. the bisection method. The quantity $\|\text{shrink}(\lambda_g, \beta)\|_1$ is a monotonically decreasing function of β , and we know that β must be somewhere in the finite interval $[0, \|\lambda_g\|_1]$. ($\beta = 0$ is too small because this involves no shrinking of λ_g , and $\beta = \|\lambda_g\|_1$ is too big because this value would shrink λ_g to zero magnitude.) This interval serves as input to the root-finding algorithm.

After solving Eq. (I.10) for β , the projection operation in Eq. (I.6) is replaced by shrinkage

$$\begin{aligned} \text{prox}_{\sigma\phi_{gc}^*}(\lambda_g) &= \lambda_g - \text{shrink}(\lambda_g, \beta), \\ &= \frac{\beta\lambda_g}{\max(\beta, |\lambda_g|)}, \end{aligned}$$

where the second line is derived by considering the two cases where components $[\lambda_g]_i < \beta$ and $[\lambda_g]_i \geq \beta$.

Interestingly, this proximal mapping is related to the proximal mapping derived for TVLSQ in Eq. (I.5); the only difference is that β is fixed for TVLSQ, while here for TVCLSQ it depends on $\nu\gamma\sigma$ and the current iteration of f and λ .

Combining all the necessary cases and elements for CPPD-TVCLSQ results in the pseudo-code presented in Algorithm 4. The function $\text{solve}(a, b)$ means to solve equation b for variable a and return the resulting value.

Algorithm 4 Pseudocode for the CPPD-TVCLSQ inner loop at iteration k .

- 1: $f^{(k+1)} \leftarrow f^{(k)} - T \left(X^\top \lambda_s^{(k)} + \nu D^\top \lambda_g^{(k)} \right)$
 - 2: $\bar{f} \leftarrow 2f^{(k+1)} - f^{(k)}$
 - 3: $\lambda_s^{(k+1)} \leftarrow \left(\lambda_s^{(k)} + \sigma(X\bar{f} - g) \right) / (1 + \sigma)$
 - 4: $\lambda_g^+ \leftarrow \lambda_g^{(k)} + \sigma \nu D \bar{f}$
 - 5: **if** $\|\lambda_g^+\|_1 > \nu \gamma \sigma$ **then**
 - 6: $\beta^{(k+1)} \leftarrow \text{solve}(\beta, \|\text{shrink}(\lambda_g^+, \beta)\|_1 - \nu \gamma \sigma = 0)$
 - 7: $\lambda_g^{(k+1)} \leftarrow \beta^{(k+1)} \lambda_g^+ / \max(\beta^{(k+1)}, |\lambda_g^+|)$
 - 8: **else**
 - 9: $\beta^{(k+1)} \leftarrow 0$
 - 10: $\lambda_g^{(k+1)} \leftarrow 0$
 - 11: **end if**
 - 12: $y_s^{(k+1)} \leftarrow \frac{1}{\sigma}(\lambda_s^{(k)} - \lambda_s^{(k+1)}) + X \bar{f}^{(k+1)}$
 - 13: $y_g^{(k+1)} \leftarrow \frac{1}{\sigma}(\lambda_g^{(k)} - \lambda_g^{(k+1)}) + D \bar{f}^{(k+1)}$
-

- [1] Chambolle A and Pock T 2011 *J. Math. Imag. Vis.* **40** 120–145
- [2] Rockafellar R T 1970 *Convex analysis* (Princeton university press, Princeton NJ)
- [3] Sidky E Y, Jørgensen J H and Pan X 2012 *Phys. Med. Biol.* **57** 3065–3091
- [4] Boyd S, Parikh N, Chu E, Peleato B and Eckstein J 2011 *Found. Trends Mach. Learn.* **3** 1–122
- [5] Barber R F and Sidky E Y 2024 *J. Mach. Learn. Res.* **25** 1–46
- [6] He B and Yuan X 2012 *SIAM J. Imaging Sci.* **5** 119–149
- [7] Pock T and Chambolle A 2011 Diagonal preconditioning for first order primal-dual algorithms in convex optimization *International Conference on Computer Vision (ICCV 2011)* pp 1762–1769
- [8] Wirgin A 2004 *arXiv preprint math-ph/0401050*
- [9] Paige C and Saunders M A 1982 *ACM Trans. Math. Soft* **8** 43–71
- [10] Jensen T L, Jørgensen J H, Hansen P C and Jensen S H 2012 *BIT Numerical Mathematics* **52** 329–356
- [11] Candès E J, Romberg J and Tao T 2006 *IEEE Trans. Inf. Theory* **52** 489–509
- [12] Donoho D L 2006 *IEEE Trans. Inf. Theory* **52** 1289–1306
- [13] Jørgensen J S and Sidky E Y 2015 *Philos. Trans. Royal Soc. A* **373** 20140387
- [14] Lustig M, Donoho D and Pauly J M 2007 *Magn. Reson. Med.* **58** 1182–1195
- [15] Sidky E Y and Pan X 2008 *Phys. Med. Biol.* **53** 4777–4807
- [16] Graff C G and Sidky E Y 2015 *Appl. Opt.* **54** C23–C44
- [17] Reiser I and Nishikawa R M 2010 *Med. Phys.* **37** 1591–1600
- [18] Jørgensen J S, Sidky E Y and Pan X 2013 *IEEE Trans. Med. Imag.* **32** 460–473
- [19] Kahan W 1965 *Commun. ACM* **8** 40
- [20] Higham N J 2002 *Accuracy and stability of numerical algorithms, 2nd edition* (Society for Industrial and Applied Mathematics, Philadelphia, PA)
- [21] Hiriart-Urruty J B and Lemaréchal C 1993 *Convex analysis and minimization algorithms I* (Springer, Berlin, Germany)
- [22] Beck A and Teboulle M 2009 *SIAM J. Imag. Sci.* **2** 183–202
- [23] Komodakis N and Pesquet J C 2015 *IEEE Sig. Proc. Mag.* **32** 31–54
- [24] Ryu E K and Boyd S 2016 *Appl. Comput. Math* **15** 3–43
- [25] Goldstein T, Li M, Yuan X, Esser E and Baraniuk R 2013 *arXiv preprint arXiv:1305.0546*
- [26] Sidky E Y, Jørgensen J S and Pan X 2013 *Med. Phys.* **40** 031115
- [27] Barber R F and Sidky E Y 2016 *J. Mach. Learn. Res.* **17** 144:1–51
- [28] Barber R F, Sidky E Y, Schmidt T G and Pan X 2016 *Phys. Med. Biol.* **61** 3784–3818
- [29] Natterer F 1986 *The mathematics of computerized tomography* (Society for Industrial and Applied Mathematics, Philadelphia, PA)
- [30] Ramani S and Fessler J A 2012 *IEEE Trans. Med. Imag.* **31** 677–688
- [31] Wang T, Kudo H, Yamazaki F and Liu H 2019 *Phys. Med. Biol.* **64** art. no. 145006

- [32] Ong F, Uecker M and Lustig M 2019 *IEEE Trans. Med. Imaging* **39** 1646–1654
- [33] Duchi J, Shalev-Shwartz S, Singer Y and Chandra T 2008 Efficient projections onto the ℓ_1 -ball for learning in high dimensions *Proceedings of the 25th international conference on Machine learning* (ACM) pp 272–279